Microjets via Laser-Induced Tandem Bubble for Controlling Crystallization in a Micro-capillary

AN EXPERIMENTAL STUDY

Adithya Vignesh

Delft University of Technology

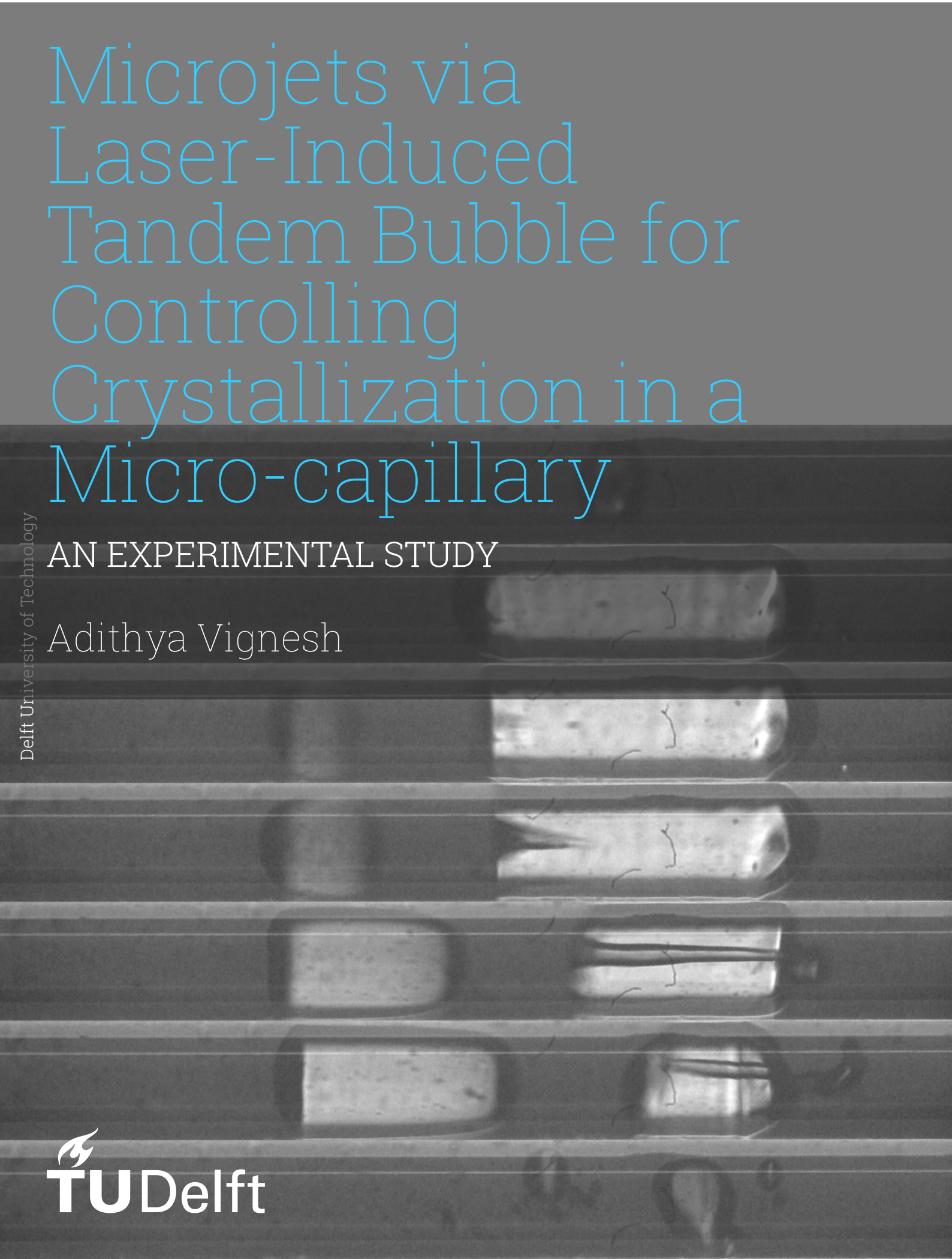

TU Delft

Microjets via Laser-Induced Tandem Bubble for Controlling Crystallization in a Micro-capillary

AN EXPERIMENTAL STUDY

by

Adithya Vignesh

to obtain the degree of Master of Science
at the Delft University of Technology,
to be defended publicly on Wednesday November 26, 2025 at 2:30 P.M.

Supervisor:	Dr. Ir. H. B. Eral
Daily Supervisor:	Dr. Ir. N. Nagalingam
Project Duration:	September, 2022 - January, 2024
Faculty:	Faculty of Mechanical Engineering, Delft

Cover: Generation and propagation of a piercing microjet as seen from high-speed imaging taken during the experiments performed in the current work

TU Delft

PREFACE

This thesis marks the completion of the academic requirements for the degree of Master of Science in Mechanical Engineering under the specialization track- Energy, Flow and Process Technology. The research work presented here was carried out at the EralLab, within the Department of Process and Energy (P&E), Faculty of 3mE, Delft University of Technology. The supervision was provided by Dr. ir. Burak Eral and Ir. N. Nagalingam whose guidance throughout the project is gratefully acknowledged.

The main focus of this thesis is to investigate the effect of laser-induced cavitation on crystal nucleation in supersaturated aqueous solutions. Confined and microfluidic systems were explored, with an emphasis on understanding how cavitation bubbles influence nucleation probability and spatial occurrence of crystallization. The motivation for this study arises from the complex interplay between fluid dynamics, phase change phenomena, and crystallization kinetics in microscale environments.

This document offers a comprehensive overview of the theoretical background, experimental methods, and observations gathered throughout the course of the research. Readers seeking an introduction to the physics of laser-induced crystallization are encouraged to begin with Chapter 1, which covers the relevant literature. Those intending to replicate the experimental setup can refer to Chapter 2 and Appendices A, B, and C, where the system design and procedures are documented in detail. The experimental findings for confined geometries are presented and discussed in Chapters 3 and 4, respectively.

I accept full responsibility for the content and structure of this report. Any feedback, comments, or constructive criticism regarding this work are welcome and will be received in the spirit of continuous learning and improvement.

The cover image of this report showcases the formation of piercing jets. This image is a direct capture from the experiments carried out in the current study.

Adithya Vignesh
Delft, November 2025

ACKNOWLEDGEMENTS

First and foremost, I wish to express my deepest gratitude to my parents, whose never-ending love and unwavering support have been the greatest constants in my life. There are truly no words that can encapsulate the sacrifices they have made to give me the opportunity to pursue higher studies abroad. It is because of their resilience, faith, and boundless encouragement that I have been able to reach this significant milestone. This work is as much theirs as it is mine.

Secondly, I would like to extend my heartfelt thanks to **Dr. Burak**, for offering me the opportunity to undertake this research. Working on a topic that is not only technically challenging but also highly relevant to industrial applications has been both stimulating and rewarding. I am especially grateful for the freedom you granted me throughout the research process, your valuable insights, and your critical yet constructive feedback. Your immense patience and genuine concern for my well-being, regularly checking in to ensure I was not overwhelmed or burnt out, meant a great deal to me, especially during difficult phases of the work.

A very special mention must go to my daily supervisor, **Nagaraj anna**, whose guidance has been invaluable from day one. You patiently introduced me to the fundamentals of this field and walked alongside me all the way to the completion of this report. Your clarity of thought, deep command over the subject, and calm, grounded demeanor made complex concepts easier to understand and the research journey far more enriching. Beyond academics, your humility and personal values have left a lasting impression on me, and I will continue to look up to you as a role model in both professional and personal spheres.

I would also like to thank **Michel**, the lab head, and the **lab technicians**, for their support in helping me acquire and relocate the components essential for setting up and carrying out my experimental work. Their assistance played a key role in ensuring that my practical work progressed smoothly. A heartfelt thanks to **Brian**, my academic coordinator, who has been a constant source of support from my very first year until now.

To my wonderful friends in Delft—**Ilambarathi, Karthi, Kakaa, Divyansh, Akul, Ajith, Achinth, Arvind, Sanga, GJ, Rajesh**, and many others whose names I may not have listed here—you have been my family away from home. Thank you all for being a pillar of support over these five years. From solving assignments together to roaming the city, cooking meals, gaming online, and simply being there in moments big and small—each memory is a treasure I will always carry with me.

As I reflect on this journey and the growth it has brought me, I feel deeply indebted to all my **Gurus** over the years. Each of you, in your own way, has helped shape the person I am today—instilling not only knowledge but also the values that guide me. This thesis is dedicated to you all, with the utmost respect and gratitude.

ABSTRACT

Primary nucleation governs the key physicochemical, mechanical, and optical properties of crystals formed from solution, yet remains a challenging process to control. This study introduces a novel approach to induce nucleation by harnessing the hydrodynamic interactions between pairs of laser-induced thermocavitation bubbles. When two cavitation bubbles are triggered in antiphase within a confined microcapillary, their interaction generates fast-moving, micron-scale liquid jets. These jets enable controlled crystallization of potassium permanganate ($KMnO_4$) at substantially lower laser energies and supersaturation levels compared to conventional single-bubble laser nucleation methods.

Using synchronized nanosecond Nd:YAG laser pulses focused inside a 200 µm capillary, we produce tandem bubbles that give rise to three distinct jetting regimes. Pinch-off, straight, and piercing. Each exhibiting progressively increasing velocity and structural coherence. High-speed imaging confirms that nucleation is reliably initiated only when the jet reaches or pierces the far interface of the primary bubble. In contrast, single-bubble cavitation fails to initiate nucleation, even at higher laser energies.

Experimental data shows a strong correlation between jet velocity and crystal yield, modeled by a power-law relation $N \propto V_{\text{jet}}^2$, indicating that localized shear at the bubble interface plays a pivotal role in triggering nucleation. These results are supported by classical nucleation theory modified to include shear-enhanced kinetics.

Overall, this work demonstrates that tandem bubble–driven microjets offer a powerful and controllable mechanism to induce crystallization in confined environments. The technique holds promise for a wide range of applications, including microfluidic crystallization, desalination and in pharmaceutical manufacturing of pills and needle-less injections.

Keywords: NPLIN, microfluidics, laser, optics, tandem bubble, microjets, crystallization, experiments.

Contents

PREFACE i

ACKNOWLEDGEMENTS ii

ABSTRACT iii

1 Introduction 1
- 1.1 Crystallization . . . 1
  - 1.1.1 Supersaturation and Solubility diagram: . . . 1
  - 1.1.2 Nucleation . . . 2
- 1.2 Non-Photochemical Laser Induced Nucleation: A Literature Review . . . 5
  - 1.2.1 Optical Kerr Effect . . . 5
  - 1.2.2 Dielectric polarization . . . 6
  - 1.2.3 Nano-Particle Heating . . . 7
- 1.3 Microjets . . . 9
- 1.4 Motivation and Research Goals . . . 10
  - 1.4.1 Research Goals . . . 10
- 1.5 Conclusion . . . 10

2 Experimental Methodology 12
- 2.1 Experimental Setup . . . 12
  - 2.1.1 Lasers . . . 13
  - 2.1.2 Cameras . . . 16
  - 2.1.3 Geometries . . . 18
- 2.2 Conclusion . . . 19

3 Tandem Bubble Experiment 20
- 3.1 Experimental Procedure . . . 20
  - 3.1.1 Solution Preparation . . . 20
  - 3.1.2 Procedure . . . 21
- 3.2 Single Bubble Experiment . . . 23
- 3.3 Pinchoff Jet Experiment . . . 25
- 3.4 Straight Jet Experiment . . . 26
- 3.5 Piercing Jet Experiment . . . 28

4 Results 30

5 Conclusion and Recommendations 36

References 38

A APPENDIX 41
- A.1 Experimental setup . . . 41
- A.2 Experimental Protocols . . . 42

B Solublity Calculation 44

List of Figures

1.1 Solubility Curve [26] . . . 2
1.2 Plot of Free energy barrier to radius of nucleation arising from the CNT [19] . . 3
1.3 Image taken from Ward et al.,[38] . . . 4
1.4 Schematic Illustration of OKE mechanism[30] . . . 6
1.5 Nucleation probabilities of KCl (S=1.06) as a function of laser intensity [12]. Solid line is the DP model prediction. Dotted line is the linear dependence. . . 7
1.6 A graphical representation of the NPH mechanism[10] . . . 8
1.7 Formation of a microjet from a collapsing bubble close to a boundary. From[39] 9
1.8 Selected images of a bubble with a strong jet driven by a nearby free surface (from Supponen et al.) [34] . . . 9

2.1 Architecture of the experimental setup. The sketch was made using a free vector graphics library for optics (http://www.gwoptics.org/ComponentLibrary/) . . 13
2.2 Laser 1 Objective lens . . . 14
2.3 Laser 2 Objective lens . . . 14
2.4 Laser 1 . . . 15
2.5 Laser 2 . . . 15
2.6 Digital Delay and Pulse Generator . . . 15
2.7 High-Speed Camera: FASTCAM NOVA 471 S16, Photron . . . 17
2.8 Low-speed camera: Imager Pro LX 16M, LaVision . . . 17
2.9 Geometries used for performing experiments . . . 18

3.1 Tandem bubble interaction with crystal formation. . . . 22
3.2 Formation of only B1 at $E_1 = 305\mu$J . . . 23
3.3 Types of jet characterized by their velocity V_{jet} . . . 24
3.4 Types of jet characterized by their velocity V_{jet} . . . 25
3.5 Time lapse of high speed microscopy images of laser induced tandem bubbles to achieve a pinchoff jet. . . . 26
3.6 Time lapse of high speed microscopy images of laser induced tandem bubbles to achieve a straight jet. . . . 27
3.7 Time lapse of high speed microscopy images of laser induced tandem bubbles to achieve a piercing jet that pierces out of the right of B1 leading to formation of islands or new bubbles. . . . 29

4.1 Incident jet velocity corresponding to its standoff distance defined for each type of jet regime. . . . 31
4.2 Incident jet velocity corresponding to its standoff distance defined for each type of jet regime. . . . 32

A.1 Experimental Setup . . . 41

List of Tables

2.1 Laser parameters. 14
2.2 Calibrated spatial resolutions for the two-camera imaging system. 17

3.1 Experimental parameters for the pinch-off jet regime. 26
3.2 Experimental parameters for the straight jet regime. 27
3.3 Experimental parameters for the piercing jet regime. 28

4.1 Probability of Crystal Formation by Jet Type 33
4.2 Statistical Summary of Crystal Yield 33

A.1 List of Optical and Imaging Components Used in the Experimental Setup . . . 42

1

Introduction

Crystallization is the most sought after separation and purification technique in the process industry. It is the process of separation by phase transition in which a pure crystalline solid state product is obtained from a solution. Both the small scale as well as the large scale industries use this process to obtain their intermediate and final products[8]. These domains includes but not limited to the food, agriculture, chemical, petrochemical, agro-chemical, pharmaceutical industries. Though crystallization is being used for many decades, the underlying mechanisms and phenomenons for the formation of crystals is still not understood completely. This is because, crystallization depends on thermodynamics, reaction kinetics, phase transformation and its associated transport phenomenon[24, 37]. Crystallization, broadly consists of two primary phenomenon:

- Nucleation
- Growth.

1.1. Crystallization

1.1.1. Supersaturation and Solubility diagram:

Supersaturation is defined as the the difference between the solute concentration and its equilibrium concentration under the same condition. Supersaturation in a solution is defined as a solution that contains more than the average solvent that can be dissolved at a given temperature[37]. For a given temperature, the supersaturation of a solution is,

$$S = \frac{c}{c_{sat}} \tag{1.1}$$

Here, S is the supersaturation, c is the solute concentration, c_{sat} is the saturation concentration for a specific temperature. Solubility diagram is a plot that represents the relationship between supersaturation and spontaneous crystallization.

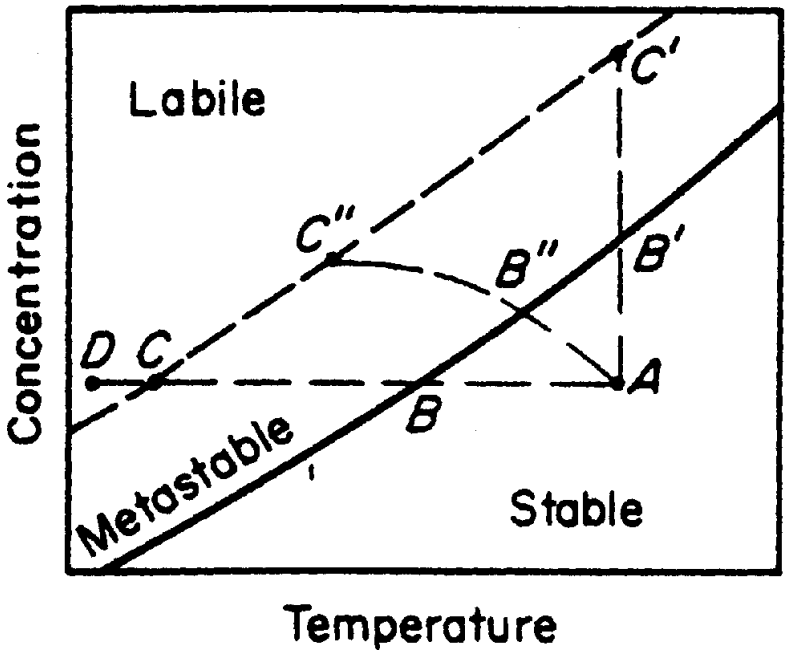

Figure 1.1: Solubility Curve [26]

- The plot is divided into stable, metastable and labile zone.
- Stable Zone: Solution is undersaturated. So crystallization does not occur.
- Labile Zone: Crystallization will occur spontaneously as the solution is supersaturated.
- Metastable Zone: It is the zone in between where the crystallization is not spontaneous but can be achieved through external physical perturbations like shock, laser, ultrasound or by agitation.
- Solid Line: solubility curve of a compound.
- Dotted Line: Super solubility curve (It is dotted as it is not well defined).[26]

1.1.2. Nucleation

Although supersaturation is a necessity for crystallization to happen, it is not adequate for a system to form crystals on its own as it requires active centres such as nuclei to develop and grow subsequently. So, nucleation can be defined as the emergence of an ordered structure of solute molecules in solution [22]. It is broadly classified into 2 types.

- Primary Nucleation: The formation of the new phase takes place spontaneously, known as homogeneous nucleation or due to the foreign particles induced in the solution such as impurities, known as heterogeneous nucleation.
- Secondary Nucleation: To enhance crystal formation, the parent crystals of the same solute are added as seeds into the solution.

Here, the mechanism for the occurrence of primary nucleation is not completely known but it can be described using two broad classification of theories.[22]

- Classical Nucleation Theory (CNT)
- Two-Step Nucleation Theory (TNS)

Classical Nucleation Theory

CNT was originally applied for condensation of a vapour into a liquid. It was later analogised to systems that undergo crystallization from supersaturated solutions. Here, small solute clusters are formed in the metastable region prior to the occurrence of primary nucleation [19]. CNT is widely used due to its analytical simplicity. It describes the nucleation as one step stochastic process dictated by the Gibbs free energy change for the phase transformation (ΔG_V) and the free energy change for the formation of a surface (ΔG_S) [36]. Therefore, the overall free energy change(ΔG) associated with the formation of these clusters is the summation of the free energy change associated with the formation of surface (ΔG_S) and the free energy change associated with the phase change (ΔG_V).

$$\Delta G = \Delta G_S + \Delta G_V \tag{1.2}$$

$$\Delta G_S = 4\pi r^2 \gamma \quad \Delta G_V = \frac{4}{3}\pi r^3 \Delta G_\nu \tag{1.3}$$

Where, r is the radius of cluster, γ is the interfacial tension between the emerging solid surface and the solvent and ΔG_ν is the free energy change of the phase transformation per unit volume.

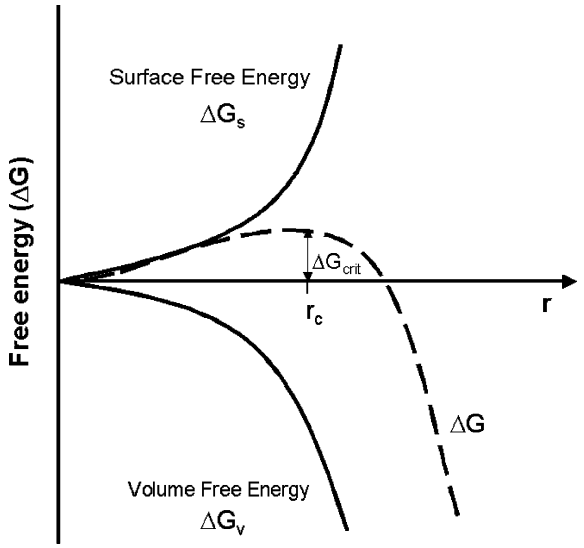

Figure 1.2: Plot of Free energy barrier to radius of nucleation arising from the CNT [19]

Here,

- ΔG_{critt} is the total free energy required to overcome for the formation of nuclei
- r_c critical radius of cluster
- Initially, when the critical radius of nuclei cluster is small, the surface energy dominates which results in the increase in overall free energy.
- When cluster size increases above r_c, the total free energy overcomes the value of ΔG_{critt} and gradually starts to decrease. Hence, the crystal growth is more energetically favoured.

CNT has numerous shortcomings as it is a simplistic model with numerous basic assumptions. It could not explain complex processes like protein crystallization experiments and nucleation in binary mixtures. This is due to the difference in composition of the clusters in such mixtures. This causes surface enrichment effects [19]. This led to the proposal of the two-step nucleation (TSN) model.

Two-Step Nucleation Theory

Two-Step Nucleation Theory was proposed after a series of experiments and molecular dynamic simulations that were done in the subsequent years. Here, the formation of a sufficiently sized amorphous pre-nucleation cluster is followed by its re-organization into an ordered structure [22]. So, it is a two barrier process where a precursor like a liquid droplet is created before the formation of amorphous clusters. This further reorganises to form crystalline clusters.

Schematic representation of the two models in comparison:

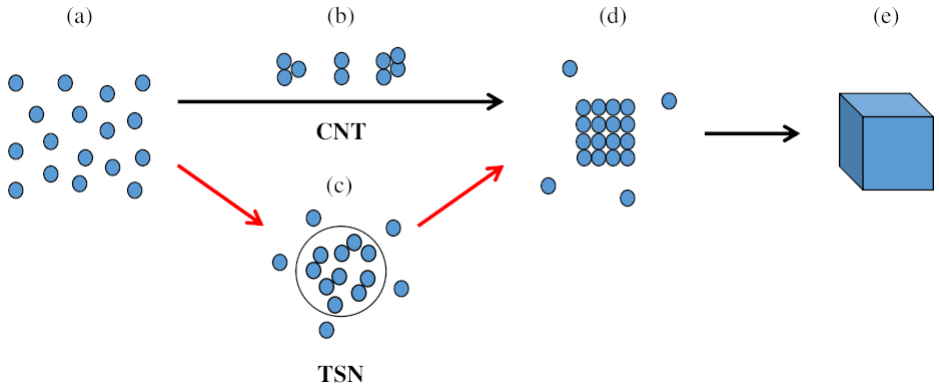

Figure 1.3: Image taken from Ward et al.,[38]

In the figure,

- (a) - distribution of solute molecules in a solution.
- (b) - ordering of pre-critical solute clusters.
- (c) - intermediate housing of amorphous solute clusters.
- (d) - Structural rearrangement to form crystalline clusters.
- (e) - final product of crystal.

Both these theories still do not completely explain nucleation. There is still more work to be done to establish a strong mathematical framework on nucleation. The primary challenge to the understanding of primary nucleation is its stochastic nature. Furthermore, numerous physical entities govern the nucleation and growth of crystals and in the end it all comes to statistics and probability. That is, there is no guarantee that nucleation will take place even if the right thermodynamic constraints are provided as it is not possible to control the location, morphology and time of the new phase that is formed. Therefore, any technique that offers a degree of control to induce nucleation would be useful [17].

Several methods have been developed in the past to induce nucleation that make use of external perturbations such as mechanical shock, electric fields or discharges and more recently, LASER.

1.2. Non-Photochemical Laser Induced Nucleation: A Literature Review

NPLIN was discovered by Garetz et al [1] in the 1990s while attempting to study second-harmonic generation in aqueous supersaturated solutions of urea $(NH_2)_2CO$. In this study, they found out that needle-shaped crystals of urea were formed when supersaturated solutions were irradiated with nano-second pulses of 1064nm laser.

The term Non-Photochemical here gives emphasis to the fact that the solution does not undergo any chemical or physical changes due to the laser. Heating due to the laser light is ruled out as absorption of water at this wavelength is small ($0.14cm_1$). Multi-photon absorption of light is also ruled out since urea in water is transparent. Spontaneous nucleation and subsequent growth of crystals was observed. This discovery lead to experiments with different solutions.

- Ward et al., reported that not all solutions undergo NPLIN. The experiments with acetamide did not yield crystals. Acetamide was chosen because of its similar solubility and structure to that of urea [7].
- Increase in laser intensities and bulk supersaturation results in the increase in nucleation probabilities. Nucleation probability is independent of wavelengths [11, 4, 6].
- Increase in laser peak intensity results in the increase of number of crystals. This was observed for glycine and KCl solutions [3, 2, 7].
- Pulse duration directly influences nucleation. Femtosecond pulse did not nucleate in aqueous solutions of KCl, NH_4Cl and CH_4N_2O whereas nanosecond pulse did nucleate. the reason is due to the vast difference in energy per pulse which is in the order of magnitude of 5 [7].
- Laser polarisation switching influences polymorphic form of simple organic molecules. This was proved for Glycine [33], L-histidine [21], carbamazepine[21] and sulfathiazole.
- In case of glycine [9] and urea[1], the nucleation probabilities improved by ageing the solutions. But the same was not true for alkali metal halides[7].
- Ward et al., [7] also noted that nucleation did not occur below a certain threshold energy. But there is no valid reasoning for the existence of such a threshold.

So, based on the observations from the experiments in the last few decades, many mechanisms were proposed.

1.2.1. Optical Kerr Effect

The first hypothesis was based on the experiments of Garetz et al., [1]. Optical Kerr Effect (OKE) states that the electric field produced by the laser induces a torque that aligns the anisotropically polarisable molecules with their most polarisable axis parallel to the direction of the incident laser light.

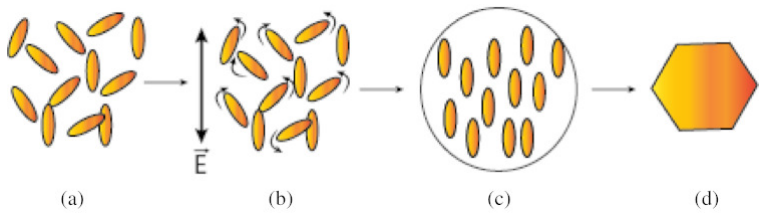

Figure 1.4: Schematic Illustration of OKE mechanism[30]

In the above figure,

- (a) - Solute molecules are randomly distributed.
- (b) - torque applied on the solute molecules due to laser induced electric field.
- (c) - solute molecules in the cluster arrange in order.
- (d) - Growth into a solid crystal.

However, through simple calculations proved by Matice et al. [4], shows that the induced torque on the urea molecules was several orders of magnitude smaller and cannot account for the reduction in nucleation time. Furthermore, this suggested that the big cluster with its collective effects of solute molecules could be the reason for the disparity. Moving forward on this work, MC simulations were performed to further examine this re-arrangement.

Simulation results showed that the electric field strength needs to be much greater that what is currently being used in NPLIN exps for nucleation to occur[15]. OKE also cannot explain NPLIN mechanism in metal halides[11, 5]. This is due to the compounds existing as ions within the solution so, in any case, under laser irradiation, these ions do not have a preferred directional orientation. This shows that the OKE model is not entirely sufficient to explain the NPLIN mechanism.

1.2.2. Dielectric polarization

This hypothesis was developed by Andrew J et al.[11, 17] to explain the NPLIN mechanism in aqueous KCl solutions. It states that the isotropic polarization of pre nucleating clusters modifies the gibbs free energy by which it becomes stable [36, 12]. This is only possible when the dielectric constant of the solute is higher than that of the solvent. The Eqn. 1.3 can be further expanded to account for laser induced electric field also. Now, the equation becomes,

$$\Delta G = 4\pi r^2\gamma + \frac{4}{3}\pi r^3(\rho k_B T \ln S + aI) \tag{1.4}$$

$$a = \frac{3\epsilon_s}{c}\left[\frac{\epsilon_p - \epsilon_s}{\epsilon_p + 2\epsilon_s}\right] \tag{1.5}$$

$$I = \frac{1}{2}c\epsilon_o E^2 \tag{1.6}$$

Here, ρ is the density of solute cluster, k_B is Boltzmann constant, T is temperature, S is super-saturation, a is effective dielectric constant, ϵ_p is relative permittivity of solute, ϵ_o is the dielectric permittivity in vacuum, ϵ_s is the relative permittivity of solvent, I is laser intensity, c is velocity

of light and E is electric flux. So this is a modified classical nucleation model. Furthermore, a relation to estimate the probability of nucleation was derived [7].

$$p_n = 1 - (e^{-mI}) \tag{1.7}$$

m is the laser independent lability.

$$m = \frac{3N_{mol}\gamma v_a}{2\pi r^3 (k_B T \ln S)} \cdot \frac{e^{-\Delta G_{crit}/k_B T}}{\int_0^{r_c} r^2 e^{-\Delta G/k_B T}\, dr} \tag{1.8}$$

N_{mol} is the total number of solute molecules only in the vicinity of the irradiated volume.

In the experiments performed with supersaturated KCl solutions, a minimum threshold of laser intensity was required to nucleate the samples[11, 12]. Now, Eqn 7., the nucleation probability was corrected in order to take into account this threshold intensity (I_0). Therefore, the equation now becomes,

$$p_n = 1 - (e^{-m(I-I_0)}) \tag{1.9}$$

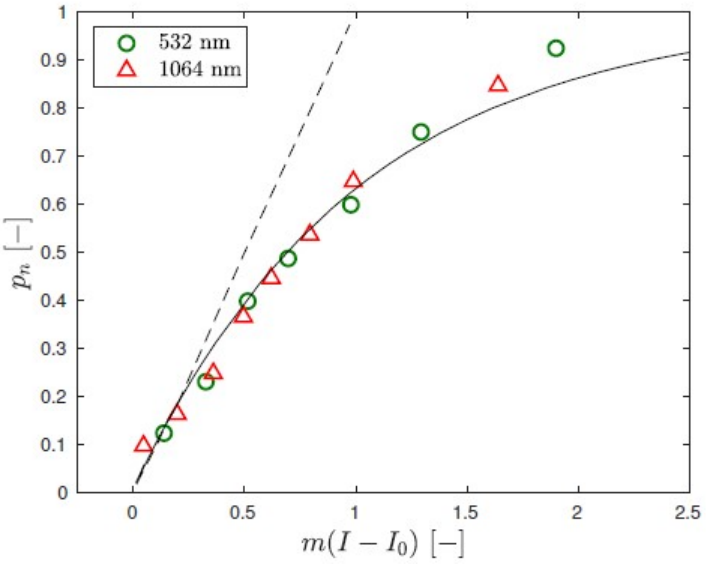

Figure 1.5: Nucleation probabilities of KCl (S=1.06) as a function of laser intensity [12]. Solid line is the DP model prediction. Dotted line is the linear dependence.

In the above plot, the DP model is in agreement with the experimental data. But the subsequent experiments on supersaturated urea solution [4, 17] and glycine[16] could not be explained by this DP model.
The above two theories cannot explain several issues. These include, an explanation for the threshold energy, why certain solutions do not exhibit NPLIN, role of filtration and pulse speed on nucleation probabilities.

1.2.3. Nano-Particle Heating

Nano particle heating refers to the heating of nano impurities that are inherently present in the solutions. NPH model proposes that the impurities inside the solution are the primary reason for nucleation when irradiated with the laser [13, 10]. According to this, the heat absorbed by the impurity is locally dissipated into the solution causing local evaporation in that vicinity leading to the formation of a vapour bubble. This hypothesis agrees with the proposed TSN model.

The rate of evaporation at the vapour-liquid interface is very high. This results in the increase in supersaturation and hence increasing the probability of nucleation and crystal growth.

This was initially put forth by Ward et al. [7] while conducting an NPLIN experiment in carbonated sugar solutions. In this study, a 5nm pulse of 532nm wavelength from a Nd:YAG laser is made to pass through a vial containing sucrose with CO_2 gas. Formation of bubbles were observed along the path of the laser beam. Threshold intensity was observed which is close to the threshold of KCl solutions. In addition to this, it was observed that the filtered sucrose solution yielded significantly less bubbles than the unfiltered solutions[7, 17, 38]. This further supports the proposal of nano particle heating.

Following this study, filtered and unfiltered solutions of KCl was tested, additional mixing of doped nano iron-oxide particles to resemble impurities were done. This further resulted in similar observation where the impurity rich solution nucleates readily and with a higher probability. The NPH model could explain and draw a relation between (i)laser intensity and probability, (ii)existence of a threshold energy and critical radius of bubble required to induce nucleation.

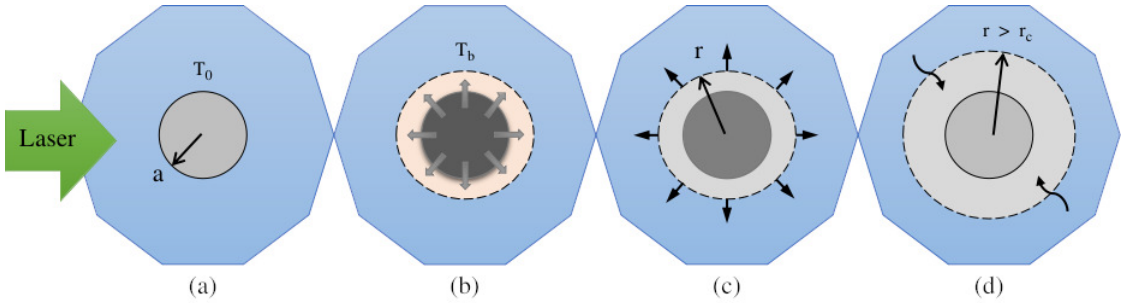

Figure 1.6: A graphical representation of the NPH mechanism[10]

From the above figure,

- (a) - For a given ambient temperature T_o, laser is irradiated and is absorbed by the nano impurity.
- (b) - heat dissipation towards the local surrounding liquid which reaches its boiling temperature T_b and starts to vaporize.
- (c) - vapour bubble expands radially outward.
- (d) - when the bubble radius r exceeds the critical radius r_c, the increase in the supersaturation at the interface will lead to formation of crystals.

1.3. Microjets

Until now, we know that the cavitation of an individual bubble can generate strong localized fluid motion and has its resulting stress fields. These have been widely used in both microfluidic systems and various biomedical applications. In an unbounded liquid environment, a cavitation bubble typically preserves its spherical symmetry throughout its growth and collapse. However, even slight asymmetries in the surrounding pressure field can break this symmetry, giving rise to anisotropic bubble dynamics and in particular, the formation of high-speed microjets [14].

Depending on the degree of anisotropy, microjets can range from very weak internal jets to strongly penetrating jets capable of exiting the bubble well before collapse. Such jetting not only redirects liquid toward the bubble's far side but also drives significant transport of fluid, suspended particles, and chemical species away from the region of bubble inception [34]. Traditionally, microjets are induced by generating bubbles near rigid surfaces, free surfaces, or by generating them in the near field of bubbles that already exists [34, 31].

Near rigid boundaries, the bubble's collapse accelerates a liquid jet toward the surface. This jet can achieve velocities of tens of meters per second and is strongly involved in surface erosion and splinters occurring from surface damage, as confirmed in classical studies of bubble–wall interactions [39].

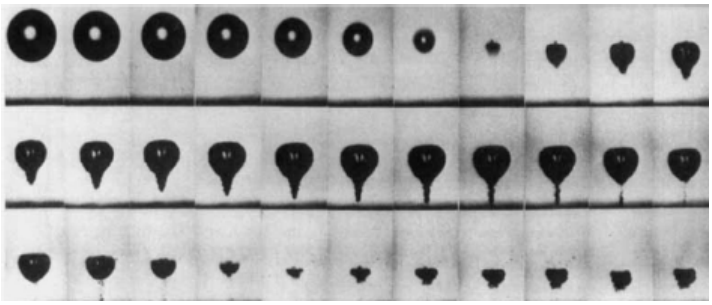

Figure 1.7: Formation of a microjet from a collapsing bubble close to a boundary. From[39]

Near free surfaces, the jet instead forms in the opposite direction—away from the boundary—often producing elongated jet structures like mushroom-cap shapes or annular vapor rings during impact, as shown in high-speed imaging by Supponen et al [34].

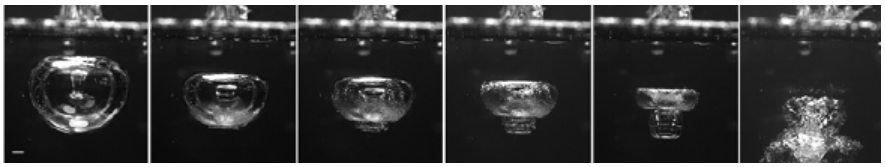

Figure 1.8: Selected images of a bubble with a strong jet driven by a nearby free surface (from Supponen et al.) [34]

In many engineered or physiological systems, however, truly free interfaces are not readily available, and rigid structures may not always be desirable due to the risk of laser and jet induced damage. Under these constraints, bubble–bubble interactions offer an attractive alternative method for inducing controlled microjet formation. Tandem or clustered bubbles can

generate strong pressure gradients that are more than those created by solid boundaries [31].

1.4. Motivation and Research Goals

The induction of jets through the interaction of multiple laser-induced bubbles has emerged as a highly versatile and non-invasive technique for manipulating fluid dynamics at the microscale. By carefully controlling the spatial and temporal characteristics of these bubbles, it becomes possible to tailor the resulting jet properties with remarkable precision. This capability has enabled a wide range of applications across several scientific and engineering domains including microrheology [29], mechanotransduction, particle manipulation, and single-cell poration [31].

The currently known laser-induced crystallization techniques, depending on the solute, may require high supersaturation or laser energy. We therefore study a novel crystallization technique that exploits the fluid flowfields associated with laser induced bubble-bubble interaction and in-situ evaporation of the solution triggering crystallization.

Therefore, this current work is focused on developing a novel method for nucleation of supersaturated aqueous $KMnO_4$ solution from the laser induced tandem bubble interaction inside a microcapillary.

The hypothesis is **"The impingement of a laser induced microjet inside a cavitation bubble initiates nucleation by inducing localized shear stress and transient concentration gradients"**.

1.4.1. Research Goals

The following are the main research goals of this study:

- Develop and validate an experimental setup capable of generating tandem cavitation bubbles inside a microcapillary.
- Conduct experiments to reliably produce piercing microjets with high repeatability.
- Systematically vary the penetrative jet velocity and the distance between laser focal points to further elucidate the underlying transport phenomena.
- Demonstrate that, for a fixed laser intensity, nucleation occurs only when a tandem bubble configuration producing a piercing jet is formed.

1.5. Conclusion

Chapter 1 has outlined the fundamental principles and challenges associated with crystallization. It emphasizes the central roles of supersaturation, nucleation, and the complex thermodynamic and kinetic factors governing crystal formation. A review of non-photochemical laser-induced nucleation (NPLIN) highlighted the significant progress made in understanding laser-mediated nucleation mechanisms. It further revealed persistent gaps and contradictions in existing theories such as the Optical Kerr Effect, dielectric polarization, and nanoparticle heating. These limitations underscore the need to explore alternative, physically well-grounded

pathways capable of delivering localized, controllable perturbations to trigger nucleation.

In this context, microjets generated by laser-induced cavitation bubbles offer a compelling direction. The ability of bubble–bubble interactions to produce highly directed, high-velocity microjets provides a non-invasive means of manipulating microscale flow fields and concentration gradients. Such jets have demonstrated utility across various microfluidic and biological applications, suggesting their untapped potential in crystallization control.

Building on this insight, the chapter introduced the central motivation for this thesis: to investigate whether the penetration induced by microjets formed through tandem laser-induced bubbles can serve as a reliable trigger for nucleation in supersaturated aqueous $KMnO4$ solutions. The research goals outlined at the end of the chapter establish the experimental and analytical framework through which this hypothesis will be examined in the subsequent chapters.

2

Experimental Methodology

This chapter outlines the experimental framework developed to investigate crystallization via laser-induced cavitation in supersaturated potassium permanganate ($KMnO_4$) solutions. It details the preparation of the solution, fabrication and handling of the capillary confinement system, and the optical setup used for generating and imaging cavitation bubbles. The chapter also describes the calibration of laser energy, synchronization of nanosecond pulses, and the high-speed imaging techniques employed to capture jet dynamics and bubble interactions. These methods collectively form the foundation for the tandem-bubble induced nucleation experiments presented in the subsequent chapters.

2.1. Experimental Setup

A general working architecture of the experimental setup is shown in Figure 2.1. The tandem bubbles are generated using two 532nm pulsed Nd: YAG laser [Table:2.1] integrated with a Digital Delay and Pulse generator [Figure:2.6].

The optical instruments used in this study were sourced from Thorlabs and comprises of lenses, mirrors, beam splitters, notch filters and a tube lens. All of them are integral to shaping and directing the laser beam within the setup towards the sample. Furthermore, a Zeiss white LED light (KL1500) is used for sample illumination.

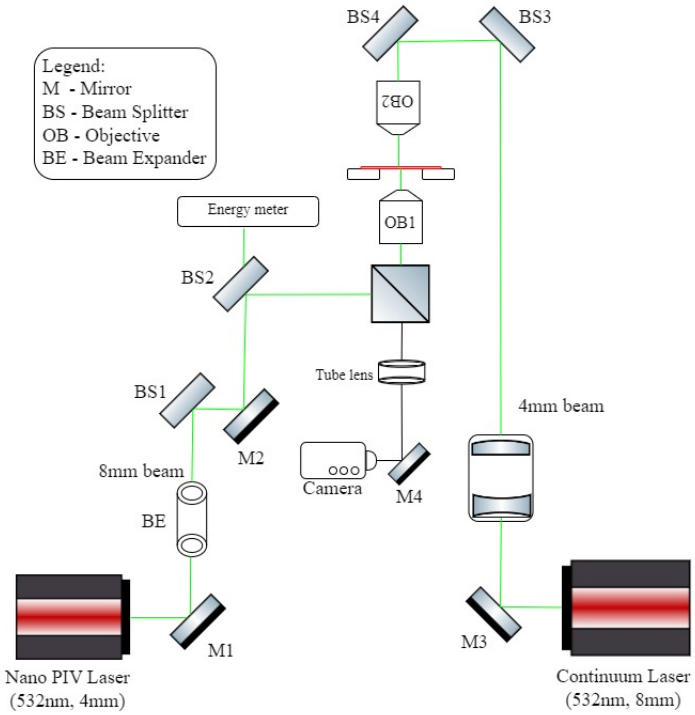

Figure 2.1: Architecture of the experimental setup. The sketch was made using a free vector graphics library for optics (http://www.gwoptics.org/ComponentLibrary/)

An infinity-corrected 20× objective (Plan Fluor, Nikon) with a numerical aperture (NA) of 0.5 is employed for Laser 1 [Figure:2.2]. Referred to as the primary objective. The relatively high NA enables efficient focusing of the laser pulse into the microcapillary, thereby ensuring reliable bubble generation. For Laser 2, an 8× objective (Plan Apochromat, Carl Zeiss) with an NA of 0.1 is used [Figure:2.3]. Referred to as the secondary objective. It provides a wider focal volume suitable for forming the secondary bubble required for tandem-bubble interaction. The 10× objective is also utilized for imaging, as its optical design and NA offer sufficient spatial resolution to capture the bubble dynamics and microjet formation with clarity.

A notch filter positioned beneath the dichroic mirror is employed to effectively suppress any reflected or scattered laser light while allowing only the LED illumination to pass through for imaging. Downstream of the optical path, a tube lens is used to relay and focus the magnified image produced by the objective onto the camera sensor, ensuring a sharp and well-resolved visualization of the bubble dynamics.

The complete experimental setup with the components are listed in Appendix[A.1]

2.1.1. Lasers

Laser irradiation forms the core of the experimental methodology. Here, two independent lasers are employed to generate the tandem cavitation bubbles required for this study Fig.[2.4,2.5]. These lasers are configured such that their focal points can be precisely aligned within the microcapillary to achieve controlled bubble–bubble interaction. The detailed specifications of both laser systems, including wavelength, pulse duration, beam diameter, and beam quality,

Figure 2.2: Laser 1 Objective lens

Figure 2.3: Laser 2 Objective lens

are summarized in Table2.1.

Table 2.1: Laser parameters.

Parameter	**Laser 1**	**Laser 2**
Model	Nano L 90-100	Powerlite DLS 8000, Continuum
Wavelength	532 nm	532 nm
Pulse duration	5 ns	7–9 ns
Diameter at source	4 mm	9 mm
Diameter at objective	8 mm	3 mm
TEM_{00}	yes	no

The flash lamp and the Q switch of both the lasers are controlled and triggered by this delay\pulse generator with the delay in the order of microsecond[μs]. This allows precise control over their activation with microsecond[μs] level timing resolution. This configuration enables flexible operation of the laser.

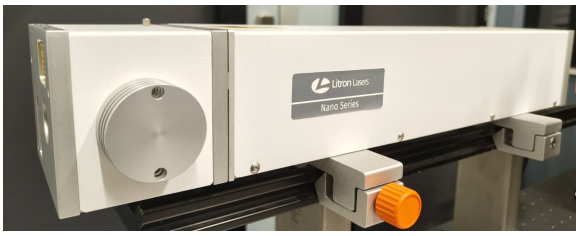

Figure 2.4: Laser 1

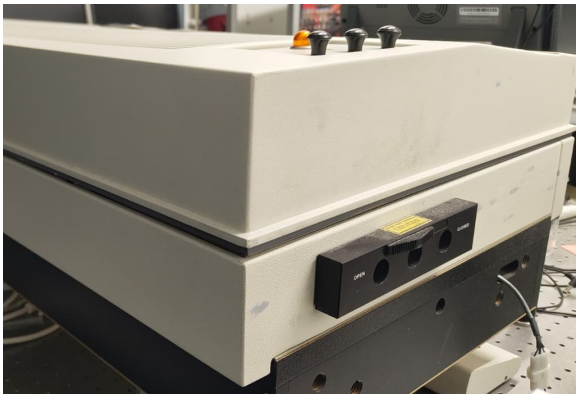

Figure 2.5: Laser 2

Figure 2.6: Digital Delay and Pulse Generator

Firstly, It can be run in a pulsed mode at a predetermined repetition rate for the main experiments where both the lasers and both the cameras have to be synchronized. Secondly, in a single-pulse, on-demand mode activated through an externally controlled trigger. Such external trigger control is essential for initial synchronization of the laser pulses with high-speed imaging and for ensuring reproducible bubble with high repeatability within the microcapillary.

Furthermore, the pulse diameter of the laser beams is adjusted to match the back-aperture of the objective lens so that the collimated beam is neither clipped nor under filled. This adjustment is achieved using a Galilean beam-expander arrangement, consisting of a negative (diverging) lens followed by a positive (converging) lens. By choosing appropriate focal lengths, the system can expand or reduce the beam diameter according to the magnification factor given by,

$$M = \left| \frac{f_2}{f_1} \right|$$

The lenses are spaced by

$$d = f_2 - f_1,$$

ensuring that a collimated beam enters and exits the expander. This compact, loss-minimizing configuration allows precise control over the pulse width delivered to the objective, ensuring optimal focusing conditions and enhancing the consistency and repeatability of thermocavitation bubble formation inside the microcapillary.

The Galilean system modifies the beam diameter according to the magnification factor:

$$M = \frac{D_{\text{out}}}{D_{\text{in}}} = \left| \frac{f_2}{f_1} \right|.$$

- If $|f_2| > |f_1|$, the beam is expanded.
- If $|f_2| < |f_1|$, the beam is reduced.

This adjustability enables fine control of the beam width before it enters the objective. For cavitation experiments, a proper beam diameter is crucial because:

- The objective's back aperture must be appropriately filled to achieve a tight, diffraction-limited focal spot.
- The energy density at the focal point determines the threshold for thermocavitation bubble formation.
- Consistent bubble generation requires stable and repeatable focusing conditions, which depend sensitively on beam geometry.

Thus, by selecting suitable focal lengths for the diverging and converging lenses in the Galilean expander, the pulse diameter can be increased to fill a high-NA objective or decreased to avoid clipping when smaller objectives are used.

Because the experimental configuration relies on two independently triggered lasers, the pulse-to-pulse energy stability of both sources was thoroughly evaluated across all operating energy levels. This characterization was essential to ensure that neither laser introduced uncontrolled variability that could influence bubble generation, bubble–bubble interactions, or the resulting hydrodynamic phenomena. For each laser, the measured fluctuations in output energy were minimal, with the maximum deviation remaining well within 2%. This high level of stability confirms that both lasers deliver reproducible energy pulses, thereby ensuring the reliability and consistency of the tandem bubble experiments conducted in this study.

2.1.2. Cameras

Camera 1, is a high-speed imaging system (FASTCAM NOVA 471 S16, Photron). It was primarily used to record the rapid growth and collapse dynamics of the thermocavitation bubbles. Due to its high frame rate and short exposure capabilities, Camera 1 enabled precise visualization of the bubble interface evolution as a function of time. This temporal resolution was essential for resolving the onset of bubble expansion, the formation of the jet, and the subsequent collapse, all of which occur on microsecond timescales.

Data acquisition and subsequent image processing for the recordings obtained from Camera 1 were carried out using the Photron FASTCAM Viewer 4 (PFV4) software package. This platform provided integrated control over high-speed image capture, synchronization settings, and frame-by-frame analysis, enabling accurate extraction of bubble interface profiles, jet formation timing, and other dynamic features relevant to the study.

Camera 2, a lower-speed but high-resolution imaging system (Imager Pro LX 16M, LaVision), was used to monitor crystallization events within a broader field of view. In contrast to Camera 1, Camera 2 was optimized for detecting the spatial formation, growth, and positioning of $KMnO_4$ crystals relative to the laser focal region and the generated bubbles. Its larger sensor area and superior pixel resolution allowed for clear identification of crystal nucleation sites and subsequent movement or aggregation, which typically evolve on much slower time

Figure 2.7: High-Speed Camera: FASTCAM NOVA 471 S16, Photron

Figure 2.8: Low-speed camera: Imager Pro LX 16M, LaVision

scales compared to bubble dynamics.

The data acquisition and image processing for the recordings obtained from Camera 2 were performed using the Lynx GigE Vision software platform. The system was operated with a shutter-time exposure of 10 ms, which provided sufficient sensitivity and contrast for reliably detecting crystal formation, growth, and spatial positioning within the microcapillary. This configuration ensured stable imaging conditions over the longer time scales associated with crystallization phenomena.

A calibration procedure was necessary to correct for deviations in the effective magnification caused by optical aberrations and other distortions in the imaging system.

- Calibration for both cameras was performed using a negative combined resolution and distortion test target (R1L1S1N, Thorlabs GmbH) [30].
- The test target was mounted on the translation stage, and the 100 µm grid pattern was brought into sharp focus individually for each camera.
- Images of the calibration grid were captured, and the number of pixels corresponding to the 100 µm spacing was measured to determine the effective spatial resolution. Refer Table:2.2

Table 2.2: Calibrated spatial resolutions for the two-camera imaging system.

Camera	Model	Calibrated Resolution (µm/px)
Camera 1 (High-speed)	FASTCAM NOVA 471 S16 (Photron)	≈ 2.0
Camera 2 (Low-speed)	Imager Pro LX 16M (LaVision)	≈ 0.74

As the two cameras operate at different time scales, it was not necessary to synchronize them with each other. Camera 1 was triggered automatically via the flash-lamp trigger of the laser system with a delay of 60–100µs achieved using a digital delay generator [Fig.2.6]. This ensured that the camera captured at least 9–10 frames prior to laser irradiation, providing a clear baseline for tracking bubble initiation and early-stage dynamics. In contrast, Camera 2 was operated manually: it was triggered immediately after the laser pulse was fired and was stopped manually approximately 5 s later.

Together, Camera 1 and Camera 2 provided a complete temporal and spatial characterization of the system, enabling simultaneous investigation of both the fast bubble dynamics and the comparatively slow crystallization phenomena central to this study.

2.1.3. Geometries

The tandem bubble experiments were performed in 200µm borosilicate glass capillaries (CM Scientific, Vitrocom Inc., New Jersey, USA) of 25mm length and round cross-section. The geometries of the experiment are given in Figure 2.9.

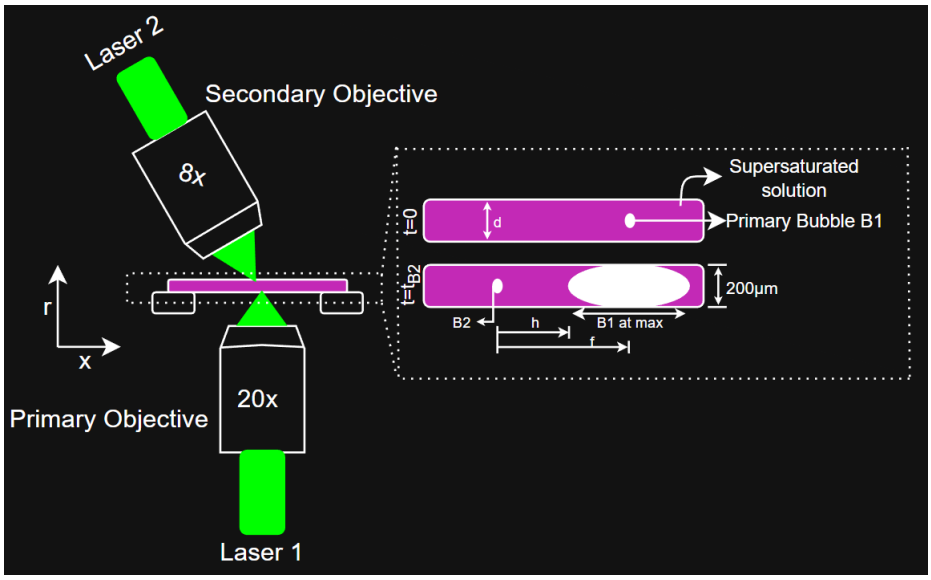

Figure 2.9: Geometries used for performing experiments

- The first thermocavitation bubble, denoted as B_1, is generated at time $t = 0$.
- The second bubble, B_2, is triggered when B_1 reaches its maximum radius $X_{1,\max}$, ensuring that the two bubbles oscillate in anti-phase.
- As B_2 expands, a liquid jet emerges within B_1 due to the hydrodynamic interaction between the bubbles.
- After both bubbles collapse and disappear, solute crystals begin to nucleate from the supersaturated solution.
- Crystal nucleation typically occurs several seconds after bubble collapse, and the crystals continue to grow on the order of minutes.
- The geometric separation between the bubbles is defined by the distance f between the laser focal points.
- The minimum distance between the center of B_2 and the nearest interface of B_1 is given by:

$$h = f - \frac{X_{1,\max}}{2}.$$

- This geometric relationship is critical because it determines the strength of the interaction and the resulting jet penetration into B_1.

2.2. Conclusion

This chapter presented a comprehensive overview of the experimental methodology developed to investigate microjet-assisted nucleation using tandem thermocavitation bubbles inside a microcapillary. The optical architecture comprising two independently controlled pulsed lasers and a dual-camera imaging system was designed. Provides precise spatial and temporal control over bubble generation while simultaneously capturing the rapid dynamics of bubble–bubble interaction and the slower crystallization phenomena that follow. Careful calibration of the optical components, cameras, and beam-shaping elements—together with detailed characterization of laser energy stability—ensured that each experiment was performed under well-defined and reproducible conditions.

The use of high-NA objectives, a Galilean beam-expander arrangement, and synchronized triggering schemes enabled consistent formation of primary and secondary cavitation bubbles at predetermined positions within the microcapillary. High-speed and low-speed imaging provided a full description of the system, ranging from microsecond-scale bubble dynamics to minute-scale crystal evolution. Additionally, the geometric framework introduced at the end of the chapter formalized the bubble configuration and interaction metrics that will be used in subsequent analysis.

Overall, the experimental platform established in this chapter forms the foundation for systematically probing the relationship between bubble-driven microjets and the initiation of crystallization in supersaturated $KMnO_4$solutions. The robustness and repeatability of the setup enable a reliable exploration of the underlying mechanisms, which will be examined in detail in the following chapter.

3

Tandem Bubble Experiment

This chapter presents the core experiments designed to test the central hypothesis: that microjets formed through laser-induced tandem bubble interactions can trigger crystallization in supersaturated $KMnO_4$ solutions. Building on the setup from Chapter 2, experiments are conducted to generate and characterize different jet types—pinch-off, straight, and piercing—by tuning laser energy and bubble spacing. High-speed imaging captures jet dynamics, while crystal formation is monitored post-collapse. The chapter begins with single-bubble control trials, followed by systematic tandem bubble experiments that highlight the role of jet velocity and interface interaction in initiating nucleation.

3.1. Experimental Procedure

3.1.1. Solution Preparation

To prepare the aqueous supersaturated $\mathrm{KMnO_4}$ solution, potassium permanganate crystals (Sigma-Aldrich, 223468) were used as the solute. All solutions were prepared in 8 mL HPLC vials. A reference solubility of 7.6 g per 100 g of water at 298 K (25 °C) was used [37], corresponding to the controlled laboratory temperature at which all experiments were conducted.

For the current study, a supersaturation ratio of $S = 1.5$ was selected, and the required mass of solute was calculated accordingly to achieve this supersaturation level in the prepared solutions. Refer Appendix[B] for solublity calculation.

- Ultrapure water (18.2 MΩ cm, ELGA Purelab) was used to prepare supersaturated $KMnO4$ solutions (223468, Sigma-Aldrich) in 8 ml vials (SF8, BGB).
- After weighing and mixing, the solution was stirred at 1000 rpm on a hot plate maintained at 333 K for one hour to accelerate dissolution.
- The solution was then placed in an oven maintained at 323 K overnight (> 12 hours) to ensure complete dissolution of salts.
- During the experiments, approximately 1.5–2 mL of the prepared supersaturated solution was transferred from the 8 mL stock vial into a smaller 2 mL HPLC vial for immediate use.

This procedure minimizes the likelihood of unwanted or premature crystallization, as only a small working volume is exposed to ambient conditions. The bulk of the solution is kept inside

a temperature-controlled oven throughout the experiments, thereby reducing thermal fluctuations and maintaining a stable supersaturation state. By limiting repeated handling of the main stock solution, this approach improves the consistency and reproducibility of the experimental results.

3.1.2. Procedure

Once the supersaturated solution of $KMnO4$ is prepared and transferred to a 2 ml HPLC vial, it is placed on the hot-plate with constant strring. Then,

- A fresh microcapillary is used for each experimental trial to ensure reproducibility and prevent cross-contamination.
- The warm solution is transferred from the hot plate to the capillary using a micropipette. Maintaining the solution at an elevated temperature helps to avoid spontaneous nucleation during handling.
- After filling, both ends of the capillary are sealed with small droplets of silicone oil (378321, Sigma-Aldrich) to prevent evaporation and maintain a stable solution concentration.
- The detailed, step-by-step experimental protocol followed during each trial is provided in Appendix[A.2].

For the laser trials,

- The vapor bubbles B_1 and B_2 are generated using Laser 1 and Laser 2, respectively, as illustrated in Figure:2.9.
- The key parameters governing the bubble dynamics and the resulting jet characteristics are:
  - the absorbed laser energies E_1 and E_2, which determine the maximum bubble sizes $X_{1,max}$ and $X_{2,max}$,
  - the standoff distance h between the bubbles at the moment of B_2 formation,
  - the time delay (phase difference) between the initiation times of the two bubbles.
- In all the trials, the bubbles are maintained in an antiphase configuration [40], such that bubble t_{B2} is generated precisely when bubble B_1 reaches its maximum length $X_{1,max}$.
- The bubble formation times are denoted as t_{B_1} and t_{B_2}, with $t_{B_1} = 0\mu$s.
- The standoff distance h is defined only at $t = t_{B_2}$ and is controlled by adjusting the separation between the two laser foci (f).
- The geometric relation governing h is

$$h = f - \frac{X_{1,max}}{2}.$$

- Prior to each experiment, the following parameters are fixed:

$$d, \quad f, \quad E_1, \quad E_2, \quad S$$

  where S is the liquid supersaturation level.
- The experimentally observed quantities are:
  - the jet evolution (including jet velocity), and

– the number of crystals formed.

Owing to the high absorption coefficient of the $KMnO4$ solution (> 1000 cm^{-1}), the incident laser energy is converted rapidly into localized thermal energy, ensuring that the interaction remains highly confined both spatially and temporally. This strong absorption not only facilitates efficient bubble formation at relatively modest pulse energies but also minimizes unwanted propagation of the beam beyond the focal region.. Details of the protocol before, during and after laser irradiations are provided in the appendix [A.2].

Figure3.1 highlights the two principal timescales of interest. The high-speed camera, operating at 112500 fps, resolves events occurring within tens of microseconds, including the growth and collapse of the primary bubble B_1, the initiation of the secondary bubble B_2, and the emergence of the penetrating jet. In contrast, crystal formation and growth occur over seconds, and are therefore captured using a low-speed camera operating at 3 fps. This dual-camera configuration allows accurate visualization of both the rapid hydrodynamic events and the subsequent crystallization processes.

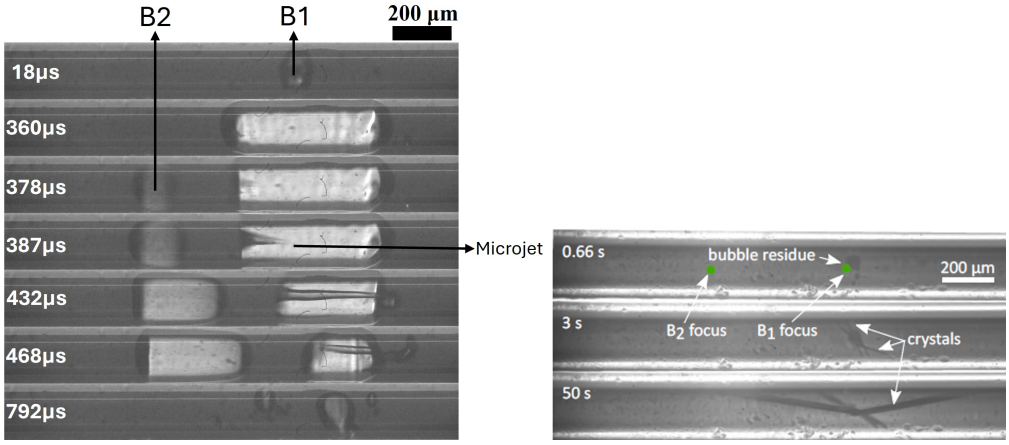

Figure 3.1: Tandem bubble interaction with crystal formation.

Figure3.1 further provides a detailed view of tandem bubble formation. As explained briefly before, the primary bubble, B_1, is generated at $t_{B_1} = 0\,\mu$s and expands to its maximum radius $X_{1,max}$. When this maximum size is reached, the secondary bubble B_2 is initiated at $t_{B_2} = 240\mu$s, thereby establishing an antiphase configuration. As B_2 expands, a strong liquid jet develops within B_1 along the axis connecting the center positions of the two bubbles. This jet accelerates rapidly and eventually pierces the right interface of B_1, producing additional small vapor cavities.

Once both bubbles collapse, the remnants of the tandem bubble interaction forms one or more residual bubbles. These residual bubbles either coalesce into a single vapor pocket or dissolve gradually over millisecond-to-second timescales, depending on their size. The collapse and the preceding jet impact cause strong solute redistribution, creating localized regions of supersaturation or concentration gradients near the residual bubble interfaces.

Crystals of optically detectable size begin to appear within a few seconds after bubble collapse,

typically forming around the residual bubbles. Their appearance suggests that the hydrodynamic effects induced by bubble oscillation and jet penetration significantly perturb the local solute field, driving the solution momentarily into a metastable state favorable for heterogeneous or pseudo-homogeneous nucleation.

Overall, the temporal and spatial correlation between jet formation, bubble collapse, and subsequent crystal emergence highlights the central hypothesis of NPLIN study: that controlled cavitation events can act as a physical trigger for nucleation in supersaturated solutions. The combination of high-speed and low-speed imaging provides a unified view of these multiscale processes, enabling a systematic investigation of how microjet dynamics influence crystallization under well-defined experimental conditions.

Having outlined the general procedure followed in each experimental trial, we now turn our attention to the core experiments of this study and examine their results and the insights gained from the observed bubble dynamics and crystallization behaviour.

3.2. Single Bubble Experiment

Before proceeding to the tandem bubble experiments, a series of control trials was performed to determine whether a single cavitation bubble is sufficient to induce crystallization under the same conditions used in this study. Firstly, ten experiments were conducted in which only bubble B_1 was generated at an energy $E_1 = 157\mu$J, while all other experimental parameters were kept identical to those used in the tandem-bubble trials. In none of these trials did crystal growth occur, indicating that the creation of a single bubble is insufficient to drive crystallization in the supersaturated solution.

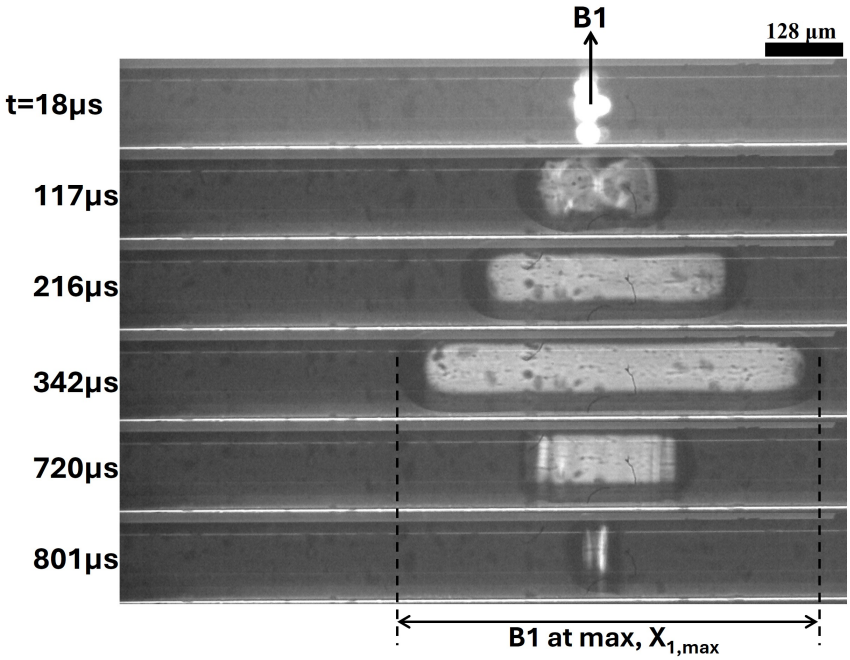

Figure 3.2: Formation of only B1 at $E_1 = 305\mu$J

To further investigate whether higher input energy could induce nucleation through a more violent single-bubble collapse, an additional ten trials were performed with nearly double the laser energy, $E_1 = 305\mu$J. Even under these intensified conditions, no evidence of nucleation was observed. These results collectively demonstrate that, under the canonical experimental conditions employed in this work, single-bubble cavitation even at elevated energies does not trigger crystallization. Figure3.2 shows the Time lapse of high speed microscopy images of laser induced primary bubble B1.

We therefore attribute the onset of crystal nucleation to the hydrodynamic effects uniquely produced during tandem bubble interaction, particularly the formation of a high-speed micro jet. In the following sections, we analyze the jet velocity and associated flow features in greater detail to elucidate their role in initiating crystallization from the supersaturated solution.

Residence Time: After every trial, the solution is inspected for the presence of crystals after a residence time of approximately 2 minutes. This waiting period is chosen to allow sufficient time for any mechanically induced nuclei to grow to an optically detectable size, while still being short enough to avoid spontaneous or thermally driven nucleation that may occur over longer timescales in a supersaturated solution. The 2-minute interval therefore provides a consistent and reliable criterion for determining whether nucleation was triggered by the bubble dynamics in each experiment.

Jet Types

From observations from the single bubble trials, we conclude that the microjet is responsible for initiating crystallization in the supersaturated solution. Therefore, before commencing the next set of core experiments, we perform a systematic characterization of the different types of jets produced during tandem bubble formation, with a specific focus on quantifying their velocities. This classification serves as a foundation for understanding how variations in jet velocity influence the likelihood and onset of nucleation.

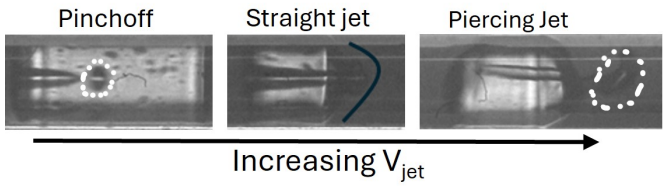

Figure 3.3: Types of jet characterized by their velocity V_{jet}

As shown in Figure3.3, the observed jets can be classified into three distinct types based on their measured jet velocity, V_{jet}:

- Pinch-off jet
- Straight jet
- Piercing jet

The identification of these jet types, and the corresponding experimental conditions required to produce them, was initially established through an iterative trial-and-error procedure in which we try and aim to gradually increasing the jet velocity V_{jet}. Throughout this process, the primary bubble energy $E_1 = 157\mu$J, the supersaturation level $S = 1.5$, and the microcapillary

diameter $d = 200\mu$m are kept constant. The remaining controllable parameters: the laser focal offset h, the axial separation of the focal points f, and the secondary laser energy E_2 were systematically adjusted to reliably generate each jet type.

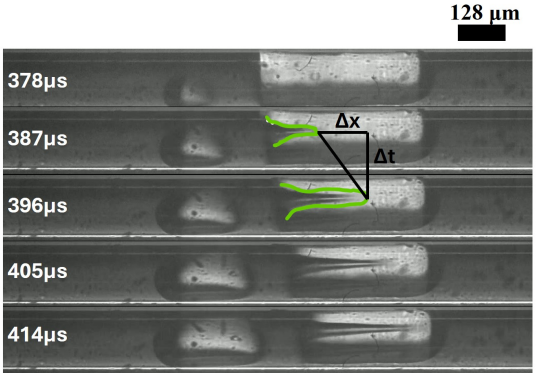

Figure 3.4: Types of jet characterized by their velocity V_{jet}

Figure3.4 presents images of the jet evolution in successive time instances. The jet-tip velocity, V_{jet}, is obtained from the rate of change of jet-tip position. Across all trials, the jet is observed to initially accelerate due to the momentum imparted by the formation and expansion of B_2. After reaching a peak velocity, the jet subsequently decelerates as surface tension counteracts the increase in interfacial area associated with jet elongation[28].

Throughout the results, tabulation, and discussion sections, the jet velocity V_{jet} is consistently referred to as the incident velocity. This quantity is defined as the velocity of the microjet at the moment it reaches the rightmost interface of the primary bubble B_1. This location is of particular importance because it represents the region where the jet impinges on and attempts to penetrate the B_1 interface. Consequently, it is at this interface that the strongest local shear stresses are generated.

Once the conditions for a specific jet category were identified, all relevant experimental parameters that were arrived through trial and error procedure were fixed, and a set of ten independent trials was conducted for each jet type. This ensured that the observed jet behaviour and subsequent crystallization outcomes were reproducible and statistically representative. The resulting classification thus provides a consistent framework for analyzing the relationship between jet dynamics and nucleation behaviour in the supersaturated solution.

3.3. Pinchoff Jet Experiment

As demonstrated earlier, nucleation and subsequent crystallization does not occur when only B_1 is generated. Even when the laser energy used to form B_1 is doubled relative to standard operating conditions. We therefore introduce the second laser pulse to generate bubble B_2 at the moment when B_1 reaches its maximum axial extent, $X_{1,\text{max}}$.

At very low jet velocities, which represent the weakest form of bubble–bubble interaction, the resulting microjet is observed to fragment into a series of small droplets within the interior of B_1. These droplets evaporate rapidly and vanish before the collapse of B_1, indicating that the

Table 3.1: Experimental parameters for the pinch-off jet regime.

Parameter	Value
Supersaturation ratio, S	1.5
Capillary diameter, d	200μm
Focal separation, f	315px $(= 630\mu$m$)$
Energy for generating B_1, E_1	157μJ
Energy for generating B_2, E_2	8.6μJ

jet lacks the momentum necessary to traverse or deform the far side interface of B_1 in a sustained manner. The full sequence of jet propagation, pinch-off, and the subsequent collapse of B_1 is presented in Figure3.5. The experimental parameters used for this set of pinch-off jet trials are summarized in Table 3.1.

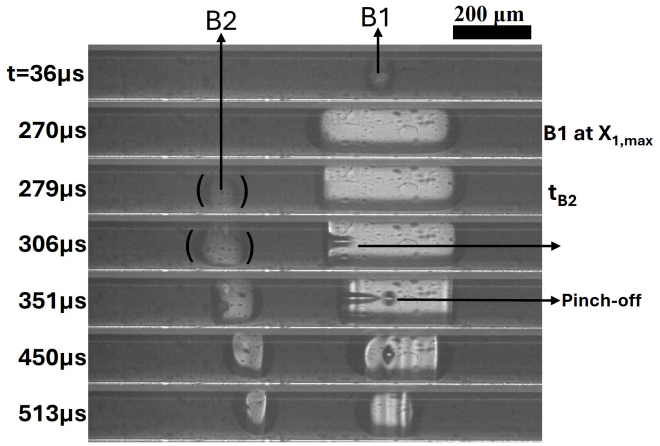

Figure 3.5: Time lapse of high speed microscopy images of laser induced tandem bubbles to achieve a pinchoff jet.

The incident jet velocity for the pinch-off regime ranges from $2.7\mathrm{m/s}$ to $6.75\mathrm{m/s}$. Notably, this velocity interval aligns well with the satellite-free drop generation range reported in the literature[35], indicating that the observed pinch-off dynamics are consistent with previously established jetting behavior.

This behaviour serves as the baseline case for weak jetting interactions and is contrasted in later sections with higher-velocity jets capable of interface deformation, penetration, and ultimately, crystal nucleation.

3.4. Straight Jet Experiment

As the incident jet velocity is increased beyond the pinch-off range, the jet behavior transitions into what we identify as the straight jet regime. In this regime, the microjet possesses sufficient momentum to propagate cleanly across the interior of bubble B_1 and reach its rightmost interface. However, its kinetic energy remains just below the threshold required to rupture or pierce the bubble surface. As a result, the jet maintains a coherent, elongated structure without breaking into droplets. Its impact on the B_1 interface generates appreciable shear and interface deformation without penetrating to the other side.

This increase in incident jet velocity is achieved experimentally by raising the energy input of the second laser, which directly enhances the strength of bubble B_2 and the resulting jet momentum. In addition to adjusting the laser energy, the focal separation f between the two laser spots is reduced, thereby decreasing the standoff distance h during each trial. The experiment parameters to generate the straight jets are given in Table3.2. A smaller separation brings the two bubbles into closer proximity, allowing the jet to interact with bubble B_1 over a shorter propagation distance. This configuration not only amplifies the momentum delivered to the B_1 interface but also increases the likelihood of maintaining a coherent jet structure upon impact. Together, these adjustments enable controlled access to the straight jet regime and facilitate systematic exploration of its associated hydrodynamic and crystallization behavior.

Table 3.2: Experimental parameters for the straight jet regime.

Parameter	Value
Supersaturation ratio, S	1.5
Capillary diameter, d	200μm
Focal separation, f	280px $(= 560\mu$m$)$
Energy for generating B_1, E_1	157μJ
Energy for generating B_2, E_2	13.6μJ

The incident jet velocity associated with the straight jet regime ranges from $6.97\mathrm{m/s}$ to $15.3\mathrm{m/s}$.

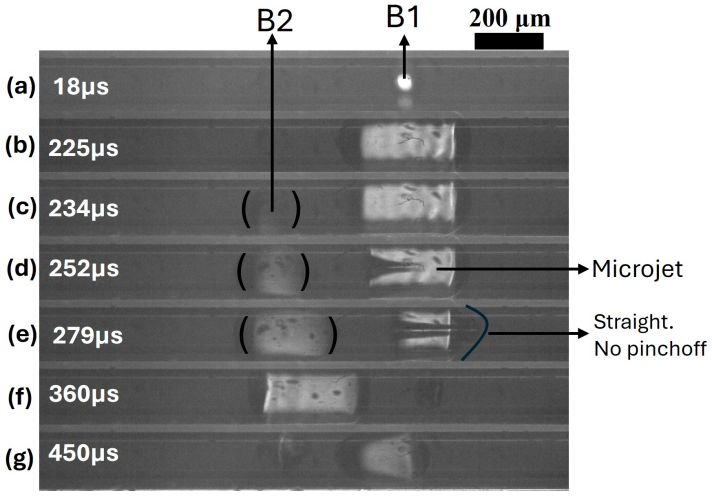

Figure 3.6: Time lapse of high speed microscopy images of laser induced tandem bubbles to achieve a straight jet.

From the Time lapse of high speed microscopy images above [Figure3.6],

(a) $t = t_{B1}$: the moment at which the laser pulse is delivered to generate bubble B_1.

(b) Bubble B_1 reaches its maximum axial extent, $X_{1\mathrm{max}}$.

(c) Initial propagation of bubble B_2 occurs immediately after B_1 attains $X_{1\mathrm{max}}$.

(d) A microjet forms and begins to propagate toward the interior of B_1.

(e) The resulting microjet remains straight, does not undergo pinch-off, and reaches the far end of B_1 without piercing its interface.

(f) Collapse phase of bubble B_1.

(g) Collapse phase of bubble B_2.

Due to the increased laser intensity and decreased bubble interaction distance, the experimental conditions become even more sensitive. Extremely small perturbations can significantly influence and alter the jet dynamics. Even a micrometre-scale impurity on the inner surface of the capillary, or the presence of a residual bubble formed while filling, can alter the local flow field in a manner that increases the jet momentum. Such unintended disturbances may push the system beyond the straight-jet threshold and lead to premature jet piercing. Careful control of the capillary cleanliness and complete removal of remnant bubbles are therefore essential to reliably accessing and characterizing the straight jet regime. The jet propagates streamlined without curvature into B1. It can deform the right bubble interface but never pierce through it.

3.5. Piercing Jet Experiment

At sufficiently high incident jet velocities, the jet dynamics transition into the piercing jet regime. In this regime, the microjet possesses enough momentum to rupture the rightmost interface of bubble B_1 and penetrate through it. This behavior marks the highest energy form of jet–bubble interaction observed in the current study and is of particular interest due to the strong shear and fluid displacement associated with jet penetration. The experimental parameters to produce a piercing jet is given in Table 3.3

Table 3.3: Experimental parameters for the piercing jet regime.

Parameter	Value
Supersaturation ratio, S	1.5
Capillary diameter, d	200 μm
Focal separation, f	265 px $(= 530$ μm$)$
Energy for generating B_1, E_1	157 μJ
Energy for generating B_2, E_2	19.8 μJ

To access this regime, similarly, the energy intensity of the second laser is further increased imparting a greater momentum to the emerging microjet. Likewise, the focal separation between the two laser spots is reduced even further which decreases the standoff distance h. Bringing the bubbles into closer proximity shortens the jet propagation path and enhances the momentum exchange at the B_1 interface. As a result, the jet arrives at the rightmost surface of B_1 with both higher velocity and greater coherence, generating significantly stronger shear stresses upon impact.

The microjet in this regime propagates sharply through B_1 and possesses sufficient momentum to rupture and pierce its rightmost interface. Upon penetration, the jet produces a secondary vapor structure on the far side of B_1, which we refer to as the island bubble. A general observation from the experimental recordings is that, within the threshold velocity region separating the straight and piercing jet regimes, the jet may occasionally pierce the B_1 interface without subsequently forming an island bubble. This behaviour suggests that such trials remain only partially outside the straight jet regime and have not fully transitioned into the piercing regime. For the sake of consistency and clarity in reporting, we therefore define the piercing jet regime strictly as those trials in which the jet penetrates the B_1 interface and successfully

generates an island bubble.

Furthermore, the combination of higher laser energy and the intensified interaction between the tandem bubbles leads to the formation of a substantially larger number of daughter bubbles. These secondary bubbles arise due to the high energy of laser and asymmetric collapse oscillation of B1 and B2.

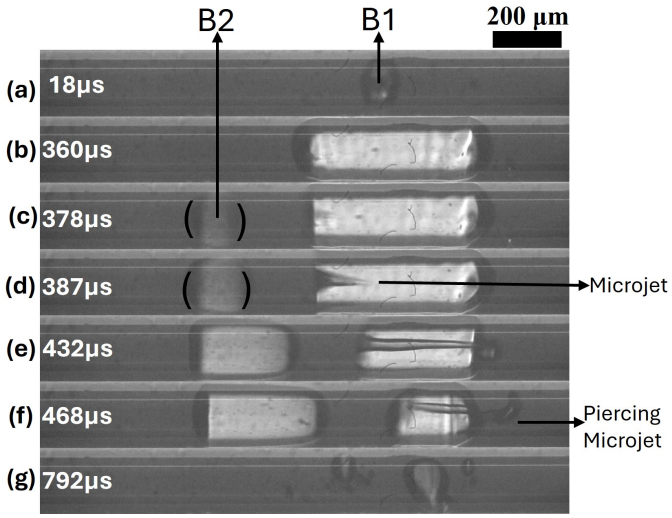

Figure 3.7: Time lapse of high speed microscopy images of laser induced tandem bubbles to achieve a piercing jet that pierces out of the right of B1 leading to formation of islands or new bubbles.

From the Time lapse of high speed microscopy images above [Figure3.7],

(a) $t = t_{B1}$: the moment at which the laser pulse is delivered to generate bubble B_1.

(b) Bubble B_1 reaches its maximum axial extent, $X_{1\text{max}}$.

(c) Bubble B_2 begins its expansion immediately after B_1 attains $X_{1\text{max}}$.

(d) A microjet forms and propagates toward the interior of B_1.

(e) The microjet continues to accelerate and approaches the opposite interface of B_1, just before breaking through.

(f) The microjet penetrates the far interface of B_1, producing a new vapor structure on the opposite side, which we refer to as an “island” bubble.

(g) Additional small daughter bubbles formed as a result of the coupled dynamics and interaction between B_1 and B_2 during this highly asymmetric collapse.

Having established the classification of the three distinct jet regimes—pinch-off, straight, and piercing—along with the corresponding experimental parameters and representative image sequences, we now possess a clear framework for interpreting the subsequent crystallization behaviour. The detailed characterization presented in the preceding section provides the necessary physical context for understanding how variations in jet momentum, coherence, and interface interaction influence nucleation outcomes. With this foundation in place, we now turn to the quantitative analysis of the experimental results, examining how jet velocity, jet type, and bubble interaction dynamics correlate with the onset and rate of crystallization in the supersaturated solution.

4

Results

The preceding chapters established the experimental framework, detailed the methodology, and classified the distinct jetting regimes arising from tandem thermocavitation bubble interactions. With these foundations in place, we now turn to a systematic presentation of the experimental results. This chapter examines how variations in jet velocity, jet type, and bubble–bubble interaction dynamics influence the onset and extent of crystallization in a supersaturated $KMnO_4$ solution.

The analysis begins by quantifying the relationship between incident jet velocity and crystal yield, followed by a statistical evaluation of nucleation probability across the three jet regimes: pinch-off, straight, and piercing. In addition, we examine the influence of jet velocity on nuclei formation through the lens of classical nucleation theory, which relates the nucleation rate J to the supersaturation S via

$$J = A \exp\left(-\frac{\Delta G^*}{kT}\right) \tag{4.1}$$

providing a theoretical framework to interpret the experimentally observed velocity-dependent crystallization behaviour.

By integrating high-speed imaging measurements, velocity characterization, and crystallization outcomes, this chapter provides a comprehensive assessment of how hydrodynamic forcing—induced by controlled jet formation—governs nucleation kinetics. These results form the basis for the discussions in the subsequent chapter.

Figure4.1 presents the plot of the incident jet velocity as a function of the standoff distance for all three types of jets. The different marker shapes and colours correspond to the 3 types of jet. Solid markers denote trials in which crystallization was observed, whereas hollow markers indicate cases where no crystals formed. As discussed previously, these crystallization outcomes are recorded after a residence time of approximately two minutes following each trial. The dotted lines shown in the figure represent a linear fit to the experimental data, yielding a slope of -0.03, which captures the overall decreasing trend of incident jet velocity with increasing standoff distance.

- **Identification of the three jet regimes:**
  - Pinch-off jets (blue region, $V_{\text{jet}} \lesssim 7\text{m/s}$): Data points cluster in the low-velocity range, corresponding to jets that lose coherence and break into droplets before reaching the far side of B_1.
  - Straight jets (red region, 7–14m/s): Points in the intermediate velocity band represent jets that remain coherent and traverse B_1, but do not possess sufficient momentum to pierce its rightmost interface.
  - Piercing jets (green region, $V_{\text{jet}} \gtrsim 14\text{m/s}$): High-velocity points indicate jets energetic enough to rupture and penetrate the B_1 interface, forming island bubbles.

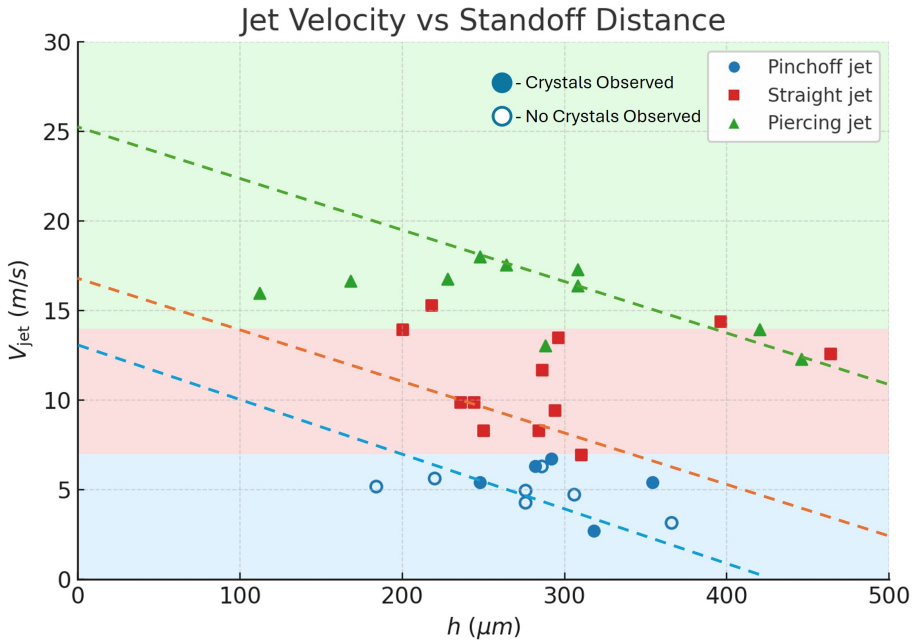

Figure 4.1: Incident jet velocity corresponding to its standoff distance defined for each type of jet regime.

- **Dependence on standoff distance:**
  - For all three jet types, jet velocity decreases approximately linearly with increasing standoff distance h, as indicated by the dashed regression lines with negative slopes. Larger separation distances reduce the hydrodynamic focusing and momentum transferred from B_2 to the jet.
- **Crystallization behavior:**
  - Pinch-off regime shows a mix of trials with and without cystals forming, reflecting inconsistent nucleation.
  - Straight jet regime shows 100% probability of crystallization nucleation.
  - Piercing jet regime exhibits a 100% probability of crystallization.

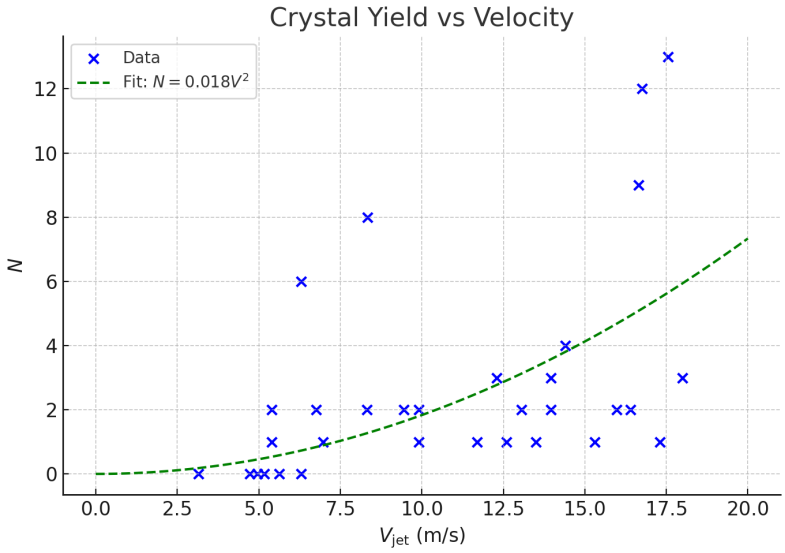

Figure 4.2: Incident jet velocity corresponding to its standoff distance defined for each type of jet regime.

We now examine how the crystal yield varies as a function of the incident jet velocity. The scatter plot in Fig.4.2 illustrates the number of crystals formed, N, as a function of the incident jet velocity V_{jet}, with each marker corresponding to an individual experimental trial.

- At lower velocities ($V_{\text{jet}} \lesssim 7\text{m/s}$), crystal formation is sparse and dominated by zero-yield events. As V_{jet} increases, the probability of nucleation rises and higher crystal counts are observed.
- A power-law model of the form $N = aV_{\text{jet}}^2$ is fit to the data, shown as the dashed green curve in the figure. The fitted expression is:

  $$N = 0.018\, V_{\text{jet}}^2.$$

  This indicates that the crystal yield grows nonlinearly with velocity, consistent with the hypothesis that higher jet momentum produces stronger shear at the B_1 interface.
- The quadratic dependence reflects the increasing kinetic energy delivered by the jet at higher velocities, which enhances shear-induced mixing and promotes nucleation in the supersaturated solution.
- While the overall trend is well captured by the V^2 fit, the data exhibit considerable spread, which is attributed to variations in jet coherence, bubble–bubble interaction timing, and local impurities within the microcapillary.
- The low-velocity points having N = 0 also reduces the apparent fit quality.

Probability of Crystallization.

The probability that a jet leads to crystal formation (defined as $N > 0$) increases monotonically with the jet type. Pinchoff jets exhibits the least crystal formation compared to the other two types, implying that the hydrodynamic stresses generated during this regime are insufficient to overcome the energetic barrier associated with primary nucleation. In contrast, straight jets nucleate crystals in 100% of the trials and similarly piercing jets show crystallization in 100% of the cases with the highest yield.

This demonstrates that the more intense and focused liquid-jet impact plays a decisive role in triggering nucleation. This trend aligns with the established understanding that stronger jet-induced shear promotes localized high supersaturation or perturbation of the interfacial boundary layer, thereby facilitating nucleation [39, 31].

Table 4.1: Probability of Crystal Formation by Jet Type

Jet Type	Probability
Pinchoff jet	0.31 (31%)
Straight jet	0.86 (86%)
Piercing jet	1.000 (100%)

Table 4.2: Statistical Summary of Crystal Yield

Jet Type	Mean	Median	Std. Dev
Pinchoff	1.85	0	3.48
Straight	2.25	1.5	2.05
Piercing	4.11	2	4.08

Statistical Yield per Jet Type.

The average number of crystals formed per trial shows a strong dependence on jet morphology. Pinchoff jets had an average yield of $N = 1.5$, reaffirming their inability to generate sufficient hydrodynamic forcing repetitively. Straight jets produce a moderate average yield of $N = 2$, with low variance, indicating that once nucleation is triggered, the subsequent crystal growth proceeds in a controlled manner. Piercing jets exhibit the highest average yield of $N = 3.25$ and a broader distribution, reflecting the combined influence of jet penetration vapor evaporation and increased shear fields. The elevated variance suggests that crystal formation in this regime is sensitive to subtle variations in jet velocity and bubble–bubble interaction, consistent with the amplification of near-wall shear stresses by microjets[27, 31].

- **Physical Interpretation.** The statistical trends highlight that nucleation probability and crystal yield are not merely functions of supersaturation, but are strongly modulated by the hydrodynamic features of the jet. Piercing jets, which deliver the largest liquid momentum flux and localized collapse-induced disturbances, are the most effective in generating nucleation sites. This is consistent with prior observations of cavitation-induced jet impact producing intense shear capable of removing adhered particles and inducing interfacial instability [27]. In the present system, these same mechanisms appear to promote phase transition from supersaturated solution to solid crystals.

The quantitative analysis confirms that controlled manipulation of jet type—via tuning experimental parameters determines crystallization outcomes. Since single-bubble experiments show no crystal formation even at higher laser energies, the crystal yields observed here underscore that the tandem-bubble configuration and its ability to generate high-velocity, structured jets is central to the nucleation mechanism. This reinforces our interpretation that nucleation in this study is a hydrodynamically driven process, dominated by jet-induced shear rather than thermal, chemical, or stochastic fluctuations.

In the following section, we further try to show from literature that the nucleation rate J is proportional to the incident velocity V_{jet}.

Classical Nucleation Theory

CNT describes the nucleation rate J as:

$$J = A \exp\left(-\frac{\Delta G^*}{kT}\right) \tag{4.2}$$

where:

- A is the kinetic prefactor,
- ΔG^* is the free energy barrier for critical nucleus formation,
- k is the Boltzmann constant,
- T is temperature.

The Gibbs free energy change $\Delta G(r)$ for forming a nucleus of radius r includes a positive surface energy and a negative volume term:

$$\Delta G(r) = 4\pi r^2 \gamma - \frac{4}{3}\pi r^3 \Delta g_v \tag{4.3}$$

Setting $\frac{d\Delta G}{dr} = 0$, we obtain the critical radius:

$$r^* = \frac{2\gamma}{\Delta g_v} \tag{4.4}$$

and substituting this back gives the critical energy barrier[23]:

$$\Delta G^* = \frac{16\pi\gamma^3}{3(\Delta g_v)^2} \tag{4.5}$$

For dilute solutions, the volume free energy Δg_v is related to supersaturation S:

$$\Delta g_v = \frac{kT \ln S}{v_m} \tag{4.6}$$

Substituting into the expression for ΔG^*:

$$\Delta G^* = \frac{16\pi\gamma^3 v_m^2}{3(kT)^3(\ln S)^2} \tag{4.7}$$

By incorporating a velocity dependent kinetic prefactor into the traditional model, we established that nucleation rate J scales linearly with shear or flow velocity under moderate conditions[25, 18]. The pre-exponential factor A in CNT accounts for frequency of successful attachment to the nucleus. It can be modified under fluid flow or shear:

$$A(v) = A_0(1 + \beta v) \tag{4.8}$$

Thus, the shear-dependent nucleation rate becomes:

$$J(v) = A_0(1 + \beta v) \exp\left(-\frac{\Delta G^*}{kT}\right) \tag{4.9}$$

This implies J and the incident velocity v are directly proportional to each other, assuming other parameters constant.

$$J(v) \propto (1 + \beta v)$$

This indicates that the nucleation rate increases with incident velocity primarily due to enhanced kinetic effects such as cluster aggregation and molecular alignment under shear flow. [20, 32]

5

Conclusion and Recommendations

This chapter brings together the key insights derived from the work presented in this thesis. A discussion of conclusions drawn from experimental observations and theoretical modeling is done. Then, it outlines targeted recommendations and future research directions that could enhance understanding and further advance the study of crystallization control via laser-induced microjets.

Conclusion

This study presents a comprehensive exploration into the influence of incident velocity on nucleation rate through the lens of Classical Nucleation Theory. By incorporating a velocity-dependent kinetic prefactor into the traditional model, we established that nucleation rate J scales linearly with shear or flow velocity under moderate conditions.

Experimental data from various crystallizing systems, including proteins and polymers, confirmed that the observed increase in nucleation rate is primarily driven by enhanced molecular mobility and collision frequency, rather than a reduction in the nucleation energy barrier. The modified theoretical model aligns well with the empirical findings and offers a physically meaningful explanation for shear-assisted nucleation.

Overall, this research highlights the critical role of dynamic fluid environments in promoting phase transitions and crystallization processes. It also provides a practical foundation for optimizing industrial crystallization operations where controlled flow conditions can be leveraged to tailor nucleation kinetics and improve process efficiency.

Recommendations

This study successfully demonstrated the influence of incident velocity and laser-induced vapor bubbles on the nucleation rate of potassium chloride using a microfluidic setup. Based on the observations, the following recommendations are proposed to extend and enhance future research:

- Since nucleation is a probabilistic event, a higher number of experimental repetitions is essential. Although ten trials per condition provided initial insights, expanding the trial count would allow more robust statistical analysis of nucleation probability and improve confidence in phase boundary estimations.
- Given the localized concentration gradients near the vapor bubble interface, a coupled

numerical model capturing both heat and solute transport would help predict spatial supersaturation profiles. Such modeling could also clarify the relationship between bubble dynamics and nucleation onset.

- The present study focused primarily on the onset of nucleation. However, time-resolved tracking of crystal growth using frame-by-frame analysis from low-speed recordings could reveal growth rate kinetics under different shear conditions, further supporting scaling to larger reactors.
- As laser-induced vapor generation may cause local heating, embedding microscale temperature sensors could help decouple thermal and kinetic contributions to nucleation enhancement, thereby isolating the effect of flow velocity more accurately.
- Future studies could also examine whether similar shear-enhanced nucleation behavior is observed in multicomponent or complex salt systems, offering insights for real-world crystallization scenarios in pharmaceutical or chemical industries.

References

[1] A Garetz et al. “Nonphotochemical, polarization-dependent, laser-induced nucleation in supersaturated aqueous urea solutions”. In: *Physical review letters 77.16, p. 3475.* (1996).

[2] Duffus C et al. “Spatial control of crystal nucleation in agarose”. In: *Journal of the American Chemical Society , 131, 11676-11677.* (2009).

[3] Hua T et al. “Microfliuidic Laser Induced Nucleation of supersaturated Aqueous Glycine Solutions”. In: *Crystal Growth and Design* (2019).

[4] Jelena Matic et al. “Intensity, wavelength, and polarization dependence of nonphotochemical laser-induced nucleation in supersaturated aqueous urea solutions”. In: *Crystal growth and design 5.4 , pp. 1565–1567.* (2005).

[5] Julien Zaccaro et al. “Nonphotochemical, laser-induced nucleation of supersaturated aqueous glycine produces unexpected γ-polymorph”. In: *Crystal Growth and Design 1.1 , pp. 5–8* (2001).

[6] Rohit Kacker et al. “Multiparameter investigation of laser-induced nucleation of supersaturated aqueous KCl solutions”. In: *Crystal Growth and Design 18.1 , pp. 312–317* (2018).

[7] Ward M et al. “Role of Impurity Nanoparticles in Laser-Induced Nucleation of Ammonium Chloride”. In: *Crystal Growth and Design* (2016).

[8] Alison Lewis et al. “Industrial crystallization: fundamentals and applications”. In: *Cambridge University Press* (2015).

[9] Julien Zaccaro et al. “Nonphotochemical, laser-induced nucleation of supersaturated aqueous glycine produces unexpected γ-polymorph”. In: *Crystal Growth and Design 1.1 , pp. 5–8.* (2001).

[10] Martin R Ward et al. “Laser-induced nucleation of carbon dioxide bubbles”. In: *The Journal of chemical physics 142.14, p. 144501.* (2015).

[11] Andrew J Alexander and Philip J Camp. “Single pulse, single crystal laser-induced nucleation of potassium chloride”. In: *Crystal Growth and Design 9.2, pp. 958–963* (2009).

[12] Lee Fiona Alexander and Norbert Radacsi. “Application of electric fields for controlling crystallization”. In: *CrystEngComm 21.34 , pp. 5014–5031.* (2019).

[13] John C Bischof and Kenneth R Diller. “From Nanoparticle Heating to Thermoregulation: A Multiscale Bioheat Transfer Review”. In: *Annual review of biomedical engineering 20 , p. 301* (2018).

[14] J. R. Blake and D. C. Gibson. “Cavitation Bubbles Near Boundaries”. In: *Annual Review of Fluid Mechanics* 19 (1987), pp. 99–123. DOI: 10.1146/annurev.fl.19.010187.000531.

[15] Michael F Doherty Brandon C Knott and Baron Peters. “A simulation test of the optical Kerr mechanism for laser-induced nucleation”. In: *The Journal of chemical physics 134.15 , p. 154501.* (2011).

[16] Jelena Matic Bruce A Garetz and Allan S Myerson. “Polarization switching of crystal structure in the nonphotochemical light-induced nucleation of supersaturated aqueous glycine solutions”. In: *Physical review letters 89.17, p. 175501.* (2002).

[17] J. Chem. “Non-photochemical laser-induced nucleation”. In: (2019). DOI: 10.1063/1.5079328. URL: https://doi.org/10.1063/1.5079328.

[18] Felice De Santis, Roberto Pantani, and Giuseppe Titomanlio. “Effect of Shear Flow on Spherulitic Growth and Nucleation Rates of Polypropylene”. In: *Polymer* 98 (2016), pp. 106–113. DOI: 10.1016/j.polymer.2016.02.059. URL: https://doi.org/10.1016/j.polymer.2016.02.059.

[19] Alfred Y Lee Deniz Erdemir and Allan S Myerson. “Nucleation of crystals from solution: classical and two-step models”. In: *Accounts of chemical research 42.5* (2009).

[20] Carol Forsyth, Paul A. Mulheran, et al. “Influence of Controlled Fluid Shear on Nucleation Rates in Glycine Aqueous Solutions”. In: *Crystal Growth & Design* 15.5 (2015), pp. 2305–2312. DOI: 10.1021/cg5008878. URL: https://dx.doi.org/10.1021/cg5008878.

[21] Clair B et al. Ikni A. “Experimental demonstration of the carbamazepine crystallization from NPLIN in acetonitrile and methanol.” In: *Crystal Growth and Design* ().

[22] D. Kashchiev. “Nucleation: Basic theory with application;” in: (2000).

[23] D. Kashchiev and G. M. van Rosmalen. “Nucleation in Solutions Revisited”. In: *Crystal Research and Technology* 38.7-8 (2003), pp. 555–574. DOI: 10.1002/crat.200310070. URL: https://dx.doi.org/10.1002/crat.200310070.

[24] Korede and Nagalingam et al. In: *arXiv:2301.09434* (2023).

[25] Jin Liu and Åke C. Rasmuson. “Influence of Agitation and Fluid Shear on Primary Nucleation in Solution”. In: *Crystal Growth & Design* 13.10 (2013), pp. 4765–4776. DOI: 10.1021/cg4007636. URL: https://dx.doi.org/10.1021/cg4007636.

[26] John William Mullin. “Crystallization”. In: (2001).

[27] Claus-Dieter Ohl et al. “Surface cleaning from laser-induced cavitation bubbles”. In: *Applied Physics Letters* 89.7 (2006). :contentReference[oaicite:1]index=1, p. 074102. DOI: 10.1063/1.2337506.

[28] Ivo R. Peters et al. “Highly focused supersonic microjets: numerical simulations”. In: *Journal of Fluid Mechanics* 719 (2013), pp. 587–605. DOI: 10.1017/jfm.2013.26.

[29] P. A. Quinto-Su et al. “Manipulation and Microrheology of Carbon Nanotubes with Laser-Induced Cavitation Bubbles”. In: *Physical Review Letters* 104.1 (2010), p. 014501. DOI: 10.1103/PhysRevLett.104.014501.

[30] Aswin Raghunathan. “Exploring laser-induced cavitation for primary nucleation control”. In: *MA Thesis* (2021).

[31] G. N. Sankin, F. Yuan, and P. Zhong. “Pulsating Tandem Microbubble for Localized and Directional Single-Cell Membrane Poration”. In: *Physical Review Letters* 105.7 (2010), p. 078101. DOI: 10.1103/PhysRevLett.105.078101.

[32] Sander et al. Stroobants. “Influence of Shear on Protein Crystallization under Constant Shear Conditions”. In: *Crystal Growth & Design* 20 (2020), pp. 1876–1883. DOI: 10.1021/acs.cgd.9b01584. URL: https://dx.doi.org/10.1021/acs.cgd.9b01584.

[33] Garetz B et al Sun X. “Polarization switching of crystal structure in the nonphotochemical laserinduced nucleation of supersaturated aqueous L-histidine”. In: *Crystal Growth and Design* (2008).

[34] Outi Supponen et al. “Scaling laws for jets of single cavitation bubbles”. In: *Journal of Fluid Mechanics* 802 (2016), pp. 263–293. DOI: 10.1017/jfm.2016.463.

[35] Yoshiyuki Tagawa et al. “Highly Focused Supersonic Microjets”. In: *Physical Review X* 2.3 (2012), p. 031002. DOI: 10.1103/PhysRevX.2.031002.

[36] Nagaraj Nagalingam et al. Vikram Korede. “A review on laser-induced crystallization from solution”. In: *arXiv:2301.09434v1* (2023).

[37] Ph.D. W. M. Haynes. “CRC Handbook of Chemistry and Physics”. In: (2017).

[38] Martin Robert Ward. “Non-photochemical laser-induced nucleation (NPLIN): An experimental investigation of crystal nucleation”. In: (2014).

[39] Leen van Wijngaarden. “Mechanics of Collapsing Cavitation Bubbles”. In: *Ultrasonics Sonochemistry* 29 (2016), pp. 524–527. DOI: 10.1016/j.ultsonch.2015.04.006.

[40] Fang Yuan, Georgy Sankin, and Pei Zhong. “Dynamics of tandem bubble interaction in a microfluidic channel”. In: *The Journal of the Acoustical Society of America* 130.5 (Nov. 2011), pp. 3339–3346. ISSN: 0001-4966. DOI: 10.1121/1.3626134. URL: https://doi.org/10.1121/1.3626134.

A

APPENDIX

A.1. Experimental setup

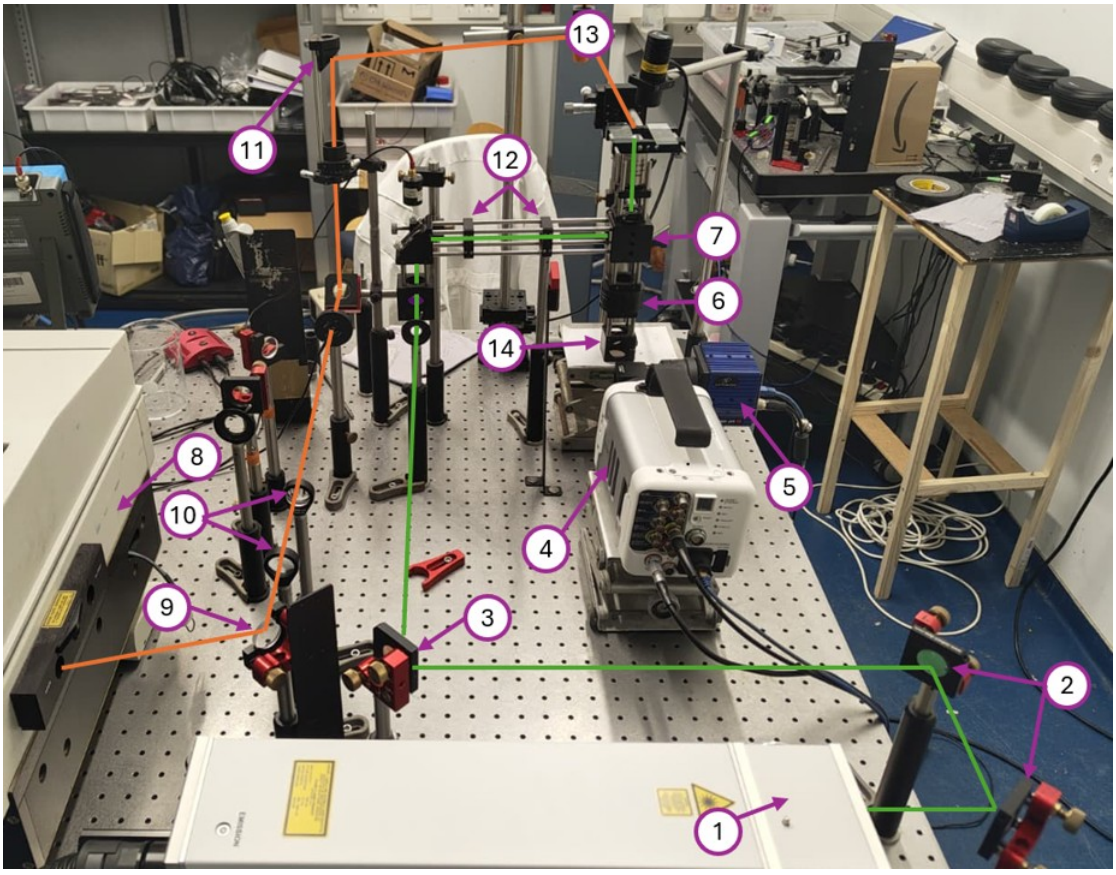

Figure A.1: Experimental Setup

The commponents are labled in table below.

Table A.1: List of Optical and Imaging Components Used in the Experimental Setup

Label	Component
1	Laser 1
2	Fully reflecting mirror
3	Fully reflecting mirror
4	High-speed camera
5	Slow-speed camera
6	Tube lens with notch filter
7	Dichroic mirror
8	Laser 2
9	Beam splitter
10	Galilean arrangement (concave and convex lens)
11	Fully reflecting mirror
12	Galilean arrangement (convex and concave lens)
13	Objective lens for Laser 2
14	Fully reflecting mirror

A.2. Experimental Protocols

SAMPLE PREPARATION

- Spread a small amount of $KMnO4$ crystals on a filter-paper-lined Petri dish and immediately close the container to avoid contamination.
- Place a clean 8 mL HPLC vial on a weighing scale, tare to zero, and transfer the required mass of $KMnO4$ from the Petri dish.
- Discard any excess $KMnO4$ safely.
- Pipette 7 mL of water into the vial and record the mass added.
- Add a magnetic stir bar and stir the solution at $25^{\circ}\mathrm{C}$ and $1500\,\mathrm{rpm}$ until the crystals begin to dissolve.
- Place the vial in an oven at $50^{\circ}\mathrm{C}$ overnight to ensure complete dissolution.

BEFORE SHOOTING LASER

- Fill the microcapillary with the supersaturated $KMnO_4$ solution. Close the capillary on either side with a drop of silicone oilb(378321, Sigma-Aldrich) to prevent evaporation.
- Place the filled capillary on the microscope sample stage and allow it to cool to room temperature. The LED illumination remains switched off during this period.
- Scan the entire length of the capillary to ensure that no crystals have formed. If the capillary is free of crystals, align it such that its longitudinal midline is centred over the objective lens.
- Trigger a few laser pulses with the shutter closed to warm up and stabilise the laser system prior to the experiment.
- Prepare the high-speed camera, low-speed camera, and oscilloscope to receive the trigger signal. The laser pulse is typically fired at approximately 7 minutes into the recording.
- The high-speed camera records for $3\,$s, while the low-speed camera continues recording for up to $2\,$min. After the first $5\,$s, the LED intensity is reduced to a minimum to prevent overexposure due to the longer integration time of the low-speed camera.

- After the recording is complete, scan the capillary from end to end to determine whether crystal(s) have formed.

AFTER SHOOTING LASER

- Record the laser pulse energy, note the room temperature, and save all images captured by the cameras.
- From the recorded high-speed images, calculate the jet propagation by measuring the pixel displacement between consecutive frames. Record the corresponding values.
- After a residence time of 2 minutes, scan the entire capillary from right to left and document whether crystals have formed, as well as the corresponding crystal yield.
- Regardless of whether crystallization occurred, discard the used solution along with the capillary, and prepare a new, clean capillary for the next trial.
- Repeat all steps following the sample preparation procedure for each new experiment.

B

Solublity Calculation

For the present study, a supersaturation ratio of $S = 1.5$ was selected, and the required mass of solute was calculated accordingly to achieve this supersaturation level in the prepared solutions.

Given the solubility of $\mathrm{KMnO_4}$ at 298 K as

$$C_{\text{sat}} = 7.6 \text{ g per } 100 \text{ g } \mathrm{H_2O},$$

and using a supersaturation ratio of

$$S = 1.5,$$

the required concentration becomes

$$C = S \cdot C_{\text{sat}} = 1.5 \times 7.6 = 11.4 \text{ g per } 100 \text{ g } \mathrm{H_2O}.$$

For a solution prepared with 7 mL of water (approximated as 7 g), the required mass of $\mathrm{KMnO_4}$ is

$$m_{\text{salt}} = 11.4 \times \frac{7}{100} = 0.798 \text{ g}.$$

Thus, the mass of $\mathrm{KMnO_4}$ needed to achieve a supersaturation of $S = 1.5$ in 7 mL of water is 0.798 g.